Spatio-temporal characteristics of the Portevin–Le Châtelier effect in austenitic steel with twinning induced plasticity

P.D. Zavattieri [a,*], V. Savic [a], L.G. Hector Jr. [a], J.R. Fekete [a], W. Tong [b], Y. Xuan [b]

[a] General Motors Research and Development, 30500 Mound Road, Warren, MI 48090-9055, USA
[b] Dept. of Mechanical Engineering, Southern Methodist University, Dallas, TX 75275, USA

ARTICLE INFO

ABSTRACT

An experimental investigation of spatio-temporal characteristics of the Portevin–Le Châtelier (PLC) effect in austenitic steel with twinning induced plasticity (TWIP) is presented. Post-processing of high resolution digital images captured from specimens in quasi-static, room temperature tensile tests was conducted with a digital image correlation (DIC) method. This provided direct measurement of strain fields during all stages of the tests. Variable rate digital image capture, enabled with a custom image acquisition algorithm, guaranteed a suitable number of images recorded during serrations in load–time records. Nucleation, propagation, and morphology of individual PLC bands in both straight gage and tapered specimens were quantified with strain rate contours computed with a backward differentiation scheme. Time histories of strain evolution in the PLC band wakes were extracted from cumulative strain contours. Of the three types of PLC bands, only the continuously propagating Type A bands were observed. Band nucleation, which occurred at serration crests in flow curves derived from the DIC results, was not limited to regions of geometry-induced stress concentrations. Due to its importance in finite element springback predictions and to support theoretical model development of inelastic behavior in TWIP steel, we measured Young's modulus variation with strain in periodic loading–unloading tests. Implications of the experimental results for theoretical modeling of the PLC effect in TWIP steel are discussed.

© 2009 Elsevier Ltd. All rights reserved.

* Corresponding author. Tel.: +1 586 864 2451; fax: +1 586 986 0446.
  E-mail address: pablo.zavattieri@gm.com (P.D. Zavattieri).

1. Introduction

Twinning induced plasticity (TWIP) steels are austenitic (FCC) steels with a high manganese (Mn) content, e.g., ∼15–25 wt% (Larsson, 2007). As part of the family of advanced high strength steels (AHSS guildelines, 2008; Horvath and Fekete, 2004), TWIP steels exhibit very high strain hardening with a strain hardening index $n > 0.4$ (Chen et al., 2007; De Cooman et al., 2008; Allain et al., 2008), strength levels of 500–1200 MPa, (Frommeyer et al., 2003), and 60–95% elongation to fracture (Chen et al., 2007; De Cooman et al., 2008; Frommeyer et al., 2003; Grässel et al., 2000). The yield strength of these materials, which is of the order of 400 MPa, is similar to conventional high strength low alloy (HSLA) steels and advanced high strength steels (AHSS) such as dual-phase (DP) and transformation-induced plasticity (TRIP) steels (Krauss, 1990).

Microstructural changes during plastic deformation of high Mn TWIP steels involve twin formation (see Bayraktar et al. (2004) for images of intergranular twins in a high Mn austenitic steel) due to a low stacking fault energy (SFE), where $18 \text{ mJ/m}^2 < \text{SFE} < 50–80 \text{ mJ/m}^2$ (Iker et al., 2007), and planar slip (Chen et al., 2007; Allain et al., 2004a). Twinning promotes retention of the austenitic microstructure, but competes with dislocation glide by impeding dislocation motion at twin boundaries, (Bouaziz and Guelton, 2001; Allain et al., 2004a; Christian and Mahajan, 1995) and other dislocation–dislocation interactions (e.g., forest hardening) (Scott et al., 2006). Of the few theoretical models of plasticity in TWIP steels, that due to Shiekhelsouk et al. (2009), in which hardening mechanisms were explored in a low SFE TWIP steel, is noteworthy. An elastic–viscoplastic polycrystalline model based upon a rate-dependent constitutive model accounting for elasticity, thermally activated slip and twinning was developed and correlated with the experimental work of Allain et al. (2004b). It was concluded that strain hardening in TWIP steel is the result of competing hardening and softening mechanisms related to twinning. Carbon clustering due to C–Mn interactions is also thought to contribute to hardening in TWIP steels (Chen et al., 2007; De Cooman et al., 2008).

In tensile tests, some austenitic steels exhibit dynamic strain aging (DSA) (Tamhankar et al., 1958; Cho et al., 2000), which is a form of unstable plastic flow commonly attributed to solute–dislocation interactions. A microscopic-scale mechanism for DSA was first elucidated by Cottrell (1953) more than 50 years ago and subsequently refined by McCormick (1972) and Van den Beukel (1975). Mobile dislocations can be arrested by obstacles, such as forest dislocations, precipites and grain boundaries and await thermal activation to be depinned. During this wait period, the pinned dislocations can be "aged" by clouds of solute atoms that diffuse to the dislocation cores under appropriate temperatures and strain rates (Cunningham, 1999). For steels, a common explanation for DSA involves reaching a critical strain to produce adequate vacancies that allow C diffusion to pinned dislocation cores (Chen et al., 2007; Owen and Grujicic, 1998; Kim et al., 1998; Cunningham, 1999). An alternate mechanism based upon vacancy diffusion was detailed by de Almeida et al. (1998) as a result of elevated temperature (∼200–800 °C) tensile tests of austenitic steels with no significant Mn content. At the lowest and highest temperatures, DSA results from reorientation of C- and N-vacancy pairs in regions where dislocations are arrested or are decelerating, while no DSA occurs at intermediate temperatures.

The repetitive aging and depinning of dislocations due to DSA gives rise to Portevin–Le Châtelier (PLC) bands which are regions of localized plastic deformation associated with discontinuous yielding. The nucleation and motion of a PLC band is now thought of as a complex spatio-temporal instability (Kubin et al., 2002) involving the collective motion of large numbers of dislocations (Hähner 1996a,b). Load–time records and flow curves from tension tests exhibit repeated serrations associated with PLC band nucleation and propagation in contrast to Lüders bands that are typically associated with a single set of upper and lower yield points (Tong and Zhang, 2007; Kyriakides and Miller, 2000). Plastic deformation is thus discontinuous or "jerky", with a negative strain rate sensitivity (nSRS) of the flow stress (Brechet and Hutchinson, 2006). Allain et al. (2008) observed that the DSA contribution to work hardening is limited in a Fe-22Mn0.6wt%C steel and that visible defects noted on tensile specimens do not appear on stampings. Dynamic strain aging and the PLC effect have been the subjects of numerous theoretical and experimental studies of steel deformation (Shi and Northwood, 1995; de Almeida et al., 1998; Jenkins and Smith, 1969; Basinski 1957; Ilola et al., 1999; Bayraktar et al., 2004; Serajzadeh, 2003; Hong et al., 2005; de Almeida and Emygdio, 1994; Cuddy and Leslie, 1972).

Portevin–Le Châtelier bands are generically categorized into three "types." The Type A band (Pink and Kumar, 1995; Robinson, 1994), which continuously propagates across the tensile specimen, has received the most attention from the theoretical community (Faciu et al., 1998; Lebyodkin et al., 2000; Hähner et al., 2001; Klose et al., 2004a,b; Rizzi and Hahner, 2004; Ananthakrishna and Bharathi, 2004). Band nucleation is commonly thought to occur at the gripper ends of a tensile specimen since a band intersecting a grip region generates a local stress concentration due to the induced gradients in plastic strain. This allows another band to nucleate at/near the grip which then propagates away from the grip into the loaded portion of the specimen. Type B bands (Tong et al., 2005a) tend to discontinuously propagate or "hop" and hence are far less spatially correlated than the Type A bands. The Type C bands nucleate and vanish with no apparent pattern (i.e., no spatial correlation) (Tong and Zhang, 2007). Theoretical investigations of the very rich physical behavior associated with PLC bands have no doubt contributed to the extensive literature base on the PLC effect and DSA. However, band propagation rather than band nucleation has been the principle focus of most studies. In practice, DSA has an undesirable impact on material formability since nSRS limits ductility (Krajewski, 2005). Visual defects in formed parts due to surface roughening in the wakes of propagating PLC bands are often an issue, particularly in nonferrous alloys, since these surface defects cannot always be completely masked by painting (Phillips et al., 1952; Hooper, 1952).

Recently, Chen et al. (2007) and De Cooman et al. (2008) investigated PLC bands in tensile measurements of a cold rolled, annealed Fe18Mn0.6C TWIP steel using infrared thermography. The highly localized strains resulted in local temperature increases that were tracked with an infrared camera. Tensile strains were measured with a 50 mm mechanical extensometer. Serrated flow curves, which consisted of plateau regions between stress "jumps", were reported beyond 0.45 true strain. The stress jumps were attributed to the Type A PLC bands at one end of the specimen due to stress concentrations. Band propagation occurred in the intervening plateaus with a small continuous increase in flow stress which suggested some hardening outside of the bands. At large true strains (i.e., close to the end of a test), Type B bands appeared and were associated with random serrations in the flow curves (Tong and Zhang, 2007). Local temperatures increased each time a PLC band passed the measuring point reaching 110 °C at the later stages of deformation. Using measured temperature data, band strains, velocities, and strain rates were predicted. Based upon estimates of the band widths, band strain rates were predicted to be two orders of magnitude higher than the applied strain rate of 0.001 1/s. As deformation proceeded, band velocities decreased due to higher band strains and lower applied strain rates (i.e., due to the longer gage length of the specimen after additional deformation).

The present paper is an experimental investigation of spatio-temporal characteristics of the PLC effect in a commercial TWIP steel with 17.2 wt% Mn. Although other experimental methodologies such as infrared thermography (Allain et al., 2008), digital speckle interferometry and correlation (Zhang et al., 2005), and laser extensometry (Hähner et al., 2002) have been used to investigate the PLC effect, we use a state-of-the-art digital image correlation (DIC) method with a custom image acquisition algorithm to directly measure strain fields in quasi-static, room temperature tensile tests. Due to the dearth of quantitative information on PLC band nucleation in TWIP steels, both straight and tapered TWIP tensile specimens were used in the experiments. The DIC method provided a quantitative exploration of PLC band nucleation with strain rate contour maps computed on an incremental basis at high spatial resolutions. Cumulative strain fields in the vicinity of propagating bands were also displayed as color contour maps. Portevin–Le Châtelier band nucleation events were identified at specific points on flow curves computed from the strain maps using a uniaxial strain measure. The image capture algorithm allowed for a variable camera framing rate which guaranteed that a sufficient number of images of a deforming tensile specimen was recorded when serrations appeared in the load–time records. Analysis of band kinematics provided a quantitative linkage between band speed and plastic strain. Due to its importance in springback calculations in sheet stamping, Young's modulus was measured with the DIC method in both single loading and periodic loading–unloading tests to explore its sensitivity to plastic strains (Doege et al., 2002; Hoanga et al., 2008). The paper concludes with a summary of the major observations from the experiments and provide some connections between our experimental results and existing theoretical models of the PLC effect.

2. Experimental details

2.1. TWIP steel composition

TWIP steel sheet with a high Mn content was acquired from POSCO at a nominal thickness of 1.5 mm. Table 1 lists the elemental constituents by wt%. Hardness testing revealed a Rockwell hardness of 97 using a 1/16th in diameter ball and a 100 kg load.

2.2. Tensile specimen geometries

Miniature tensile specimens, with a 20 mm straight gage length, were cut from the TWIP sheet material with a precision wire electrical discharge machining (EDM) process. Specimen orientations were 0°, 45°, and 90° with respect to the rolling direction. The resulting straight gage section geometry, which is bounded by two parallel edges separated by 5 mm, is shown in Fig. 1a. All surfaces were found to be free of obvious machining defects and no measurable deviations (e.g., tapers) were found in ancillary measurements with a precision coordinate measuring machine. Fig. 1b is a schematic of the tensile specimen geometry with a 1° taper (relative to the specimen axis). Our purpose in testing the tapered specimen geometry was to determine if PLC band nucleation in the TWIP steel under investigation always occurred at either the gripper end or at the center of the specimen where the width is smallest. A thin but uniform coat of white spray paint droplets was applied to one surface of each specimen (with care taken to avoid coating the gripper sections) followed by application of black paint droplets after a short drying period. This resulted in a suitable gray scale contrast pattern for post-processing of the image data with the DIC algorithm. Premature fracture and/or delamination of the paint coating were prevented in all tests by cleaning and polishing each specimen prior to paint droplet application.

2.3. Miniature tensile stage

Unless otherwise indicated, tests of the straight and tapered TWIP specimens were conducted with a miniature screw-driven tensile stage manufactured by Kammrath-Weiss. Cross-head loads up to 10 kN can be accommodated with a maximum displacement of 25 mm. The tensile stage cross-head speed and direction were set with external controller hardware. Analog signals of the load and displacement were monitored (40 Hz) by a second computer with a custom algorithm that controlled camera image acquisition rates. Once positioned in the grips of the testing stage, a specimen was clamped with hardened steel "bite plates," and elongated to fracture. A fiber optic ring light source was positioned above each specimen to provide a sufficient illumination level for the camera sensor. The majority of the tests with the miniature stage were conducted at an average constant cross-head speed of 13 μm/s which corresponds to a nominal (logarithmic) strain rate in the 0.0005–0.001 1/s range. To explore effects at a slower cross-head speed, one test was also conducted at 7 μm/s which corresponds to a nominal strain rate in the 0.00025–0.0005 1/s range. In addition, several tests were conducted at cross-head speeds in the 0.015–15 mm/min range with an Instron 5582 materials testing machine to examine nSRS of the material.

2.4. High speed camera and image acquisition process

A Phantom 9.0 high speed digital camera from Vision Research was used to record 1632 × 1200 bitmap images (each 5.7 MB, 14 μm/pixel resolution) of one entire gage section surface of each tensile specimen during testing. An image of the experimental configuration is shown in Savic et al.

Table 1
Chemical composition of TWIP steel.

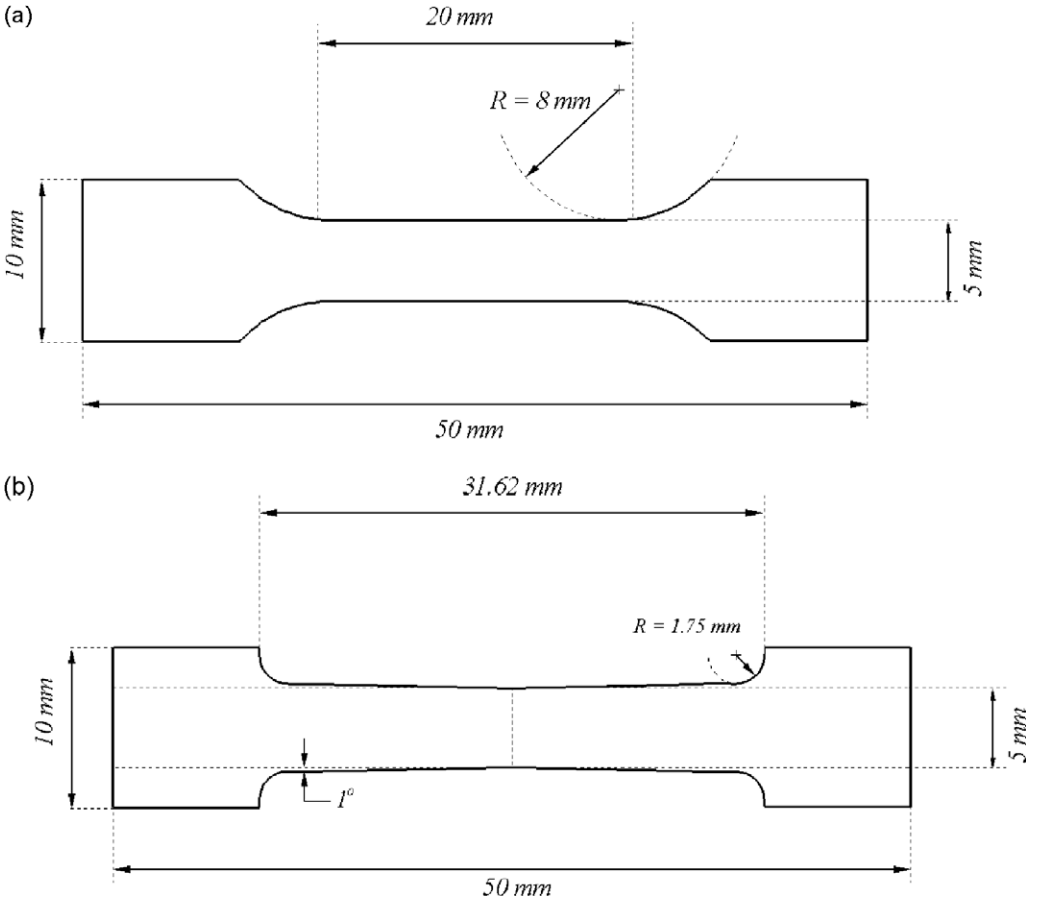| Mn	P	Si	Cr	Mo	Ni	Al	Cu	Ti	V	Nb	B	C	S
17.2	0.02	0.12	0.56	0.01	0.23	1.0	0.04	0.002	0.004	<0.002	<0.0002	0.59	0.002

(a)

(b)

Fig. 1. (a) Straight gage and (b) tapered TWIP steel tensile specimen geometries used in this study. Note that the dashed vertical line at the center of (b) denotes the thinnest gage section width of 5 mm. Nominal thickness was 1.5 mm.

(2008). As many as 650 images were captured in the 12 GB camera buffer during tensile tests in which the specimens were continuously elongated. A Nikon 105 mm telecentric lens set at a 2.8 f-stop was used for all tests. Three lens extenders provided an adequate field of view of the tensile specimen gage section through adjustment of the image magnification (about 100×). An image acquisition algorithm written in the DASYLab code directed the camera buffer to capture images of one surface at a variable rate. This rate was dictated by a set of user-chosen threshold values for load increment, decrement, and displacement based upon continuous monitoring of the analog signals from the tensile stage controller. A fourth threshold based upon an internal system clock was also utilized. Images were stored at a higher rate during periods where the load increment or decrement achieved target threshold values (e.g., ±50 N). Once an image was captured to the camera buffer, all thresholds were reset to zero and the process repeated. During periods where the loads changed less rapidly, images were captured at a lower framing rate according to selected displacement or timing thresholds. This approach to image capture is advantageous from the standpoint that it allows the user to "tune" image capture rates to acquire ample data during "specific events" in the tensile deformation process. For the TWIP steel investigated herein, a sufficient number of images was captured during serrations in tensile load–time records since load increments and decrements tended to change more quickly thereby adding images to the camera buffer at a higher rate than periods between serrations. Further details on the variable image capture algorithm may be found in Savic et al. (2008).

2.5. Digital image correlation

Digital images from the camera buffer were input to the DIC algorithm for post-processing. Once a test was completed, the images were compared in one of two ways. Cumulative correlation involved comparison of an image captured early in a test with an image captured at a later stage of the test. This process provided cumulative true strain fields and enabled quantitative study of the extent to which strains fields changed in the vicinity of a nucleating PLC band and during its subsequent propagation. Alternatively, incremental correlation resulted from comparison of temporally successive image pairs. Strain rates computed from incremental correlation enabled study of localized plasticity due to the band nucleation and propagation. Strain fields were computed from digital grids superimposed on each image and then displayed as true strain contours or maps in the post-processing DIC step. Each grid was divided into a set of square pixel subsets (typically 40×40) with a grid point at its center. The image correlation algorithm tracked the location of unique contrast features (i.e., in the spray paint pattern applied to a tensile specimen surface) corresponding to each grid point in each image, accounted for the rigid body motion of the system, and computed an average displacement and true strain value at each grid point. The errors in local in-plane displacements, rigid body rotation, and strain measurements were estimated to be 0.02 pixels, 0.02°, and 20–30 μstrains, respectively. Calibration tests to determine errors due to camera/stage alignment and DIC analysis of all test results were performed with the SDMAP3D software detailed in Tong (2005). The DIC methodology used in this study has previously been applied to: deformation measurement of dual-phase, press-hardened and fully martensitic steels in quasi-static tensile tests (Tong et al., 2005b; Savic and Hector, 2007; Savic et al., 2008, respectively); the investigation of Type B PLC bands in an Al–Mg alloy (Tong et al., 2005a); measurement of strain fields during crack growth (Tong, 2004); and the measurement of drying-induced strain fields in proton exchange fuel cell membranes (Hector et al., 2007). For additional references on the DIC methodology, the reader is referred to Tong (1997, 1998), Smith et al. (1998), and Savic et al. (2008).

True uniaxial stress was computed from

$$\sigma = \frac{Fe^{\varepsilon^{1.5}}}{WT} \tag{1}$$

where $\varepsilon^{1,5}$ is one of two true strain measures derived from the DIC contour maps, F is the cross-head load, and W and T are initial specimen width and thickness, respectively. Eq. (1) applies provided that volume constancy of plastic deformation is guaranteed and the stress state is fairly unidirectional. It has been shown that the stress–strain state in the neck region in most thin metal sheets deviates only slightly from that of uniaxial tension, despite increasingly heterogeneous strain distributions (Tong and Zhang, 2001). Eq. (1) is therefore a reasonable approximation of the uniaxial tensile stress–strain curve beyond uniform elongation to substantially larger plastic strains.

Two definitions of the average axial true strain measures were used in Eq. (1). The first is

$$\varepsilon^1 = \frac{1}{MN} \sum_{j=1}^{N} \sum_{i=1}^{M} \varepsilon(i,j), \tag{2}$$

where ε^1 is the axial strain averaged over the entire gage section (following the conventional tensile test methodology), M and N are the total numbers of grid points along the gage length and width directions, respectively, and $\varepsilon(i,j)$ is the axial strain at each grid point (i,j) obtained via DIC. The second strain measure is defined by

$$\varepsilon^5 = \varepsilon(M_0, N_0) = \max_{j=1,N}[\varepsilon(M_0,j)], \tag{3}$$

where ε^5 is the maximum axial strain corresponding to grid point (M_0, N_0) in the gage section. Local strain heterogeneities are averaged over the entire gage section in ε^1. The definitions ε^1 and ε^5, when input to Eq. (1), provide uniaxial true stress–strain curves that bound what can be considered to be the actual representation of the uniaxial true stress–strain behavior. Additional details may be found in Tong et al. (2007) and Tao et al. (2008).

3. Results

3.1. Quasi-static tensile properties

Engineering stress (S) and strain (e) curves at cross-head speeds of 0.015, 1.5 and 15 mm/min (from the Instron 5582 materials testing machine) are shown in Fig. 2 for a straight gage specimen with 0° orientation at a cross-head speed of 13 μm/s. The relationship between the curves is indicative of nSRS since a lower cross-head speed or applied strain rate leads to a higher flow strength. A more definitive demonstration of nSRS would require strain rate change tests. The peak tensile loads were in the vicinity of 7200 N.

Fig. 3 compares true stress–true strain curves from DIC analysis based upon strain measures ε^1 (red) and ε^5 (blue dashed) from Eqs. (2) and (3), respectively. These two measures differ to one extent or another with increasing strain for most metal sheet materials (Tong et al., 2005b; Savic and Hector, 2007; Savic et al., 2008). However, this is not the case here due to very limited necking of TWIP steel during tensile elongation. Also shown is the engineering stress–engineering strain (black dotted) relationship. As expected, this deviates from both true stress–true strain curves as strain increases.

Fig. 4 shows true stress–strain curves for selected TWIP specimens with 0°, 45°, and 90° orientations. Young's modulus (GPa), 0.1% and 0.2% offset yield stresses, maximum true stress (MPa) and maximum true strain prior to fracture from ε^1 for the 0°, 45°, and 90° specimens are listed in Table 2. Specimen orientation appears to have had some impact on the Young's modulus as suggested by the Fig. 4 inset and the values listed in Table 2. However, the data in Table 2 is based on a small number of samples tested. Although, there is no statistical basis for comparison of values associated with the three different orientations, the range of values reported is believed to be representative of the room temperature, quasi-static tensile properties of the TWIP steel with the chemical composition in Table 1. Ancillary tests following ASTM E8, which involved larger TWIP tensile specimens with a 0° orientation gave nearly identical results to those in Fig. 4 from DIC analysis. The inset in the same figure also suggests that the initial yield stress depends somewhat on the specimen orientation.

Great care must be taken to quantify measurement system errors during elastic loading in tensile tests. This is especially important for an optical system that is sensitive to small out-of-plane errors in the motion of the tensile stage. These errors can lead to measured elastic strains that are too small if
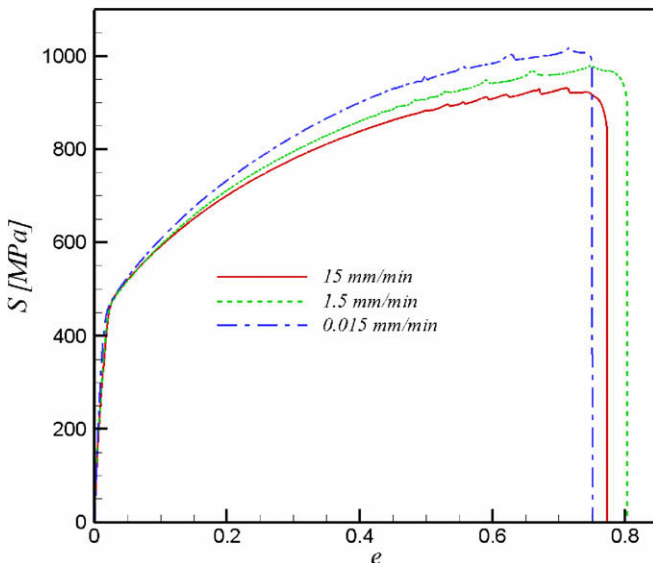

Fig. 2. Engineering stress (S) and strain (e) curves at three cross-head speeds. Negative strain rate sensitivity is suggested.
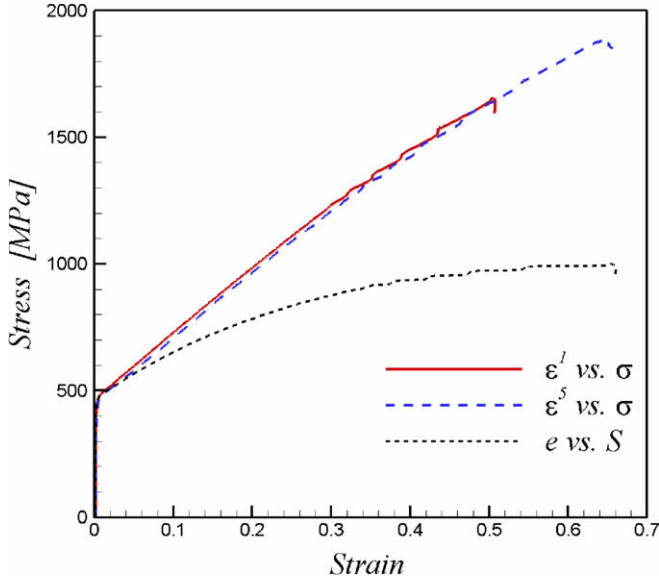
Fig. 3. True stress σ (MPa)–true strain from strain measures ε^1 and ε^5, Eqs. (2) and (3), respectively, following DIC analysis compared with engineering stress S (MPa) vs. engineering strain, e. Note that ε^1 and ε^5 are essentially identical up to a 0.5 true strain.
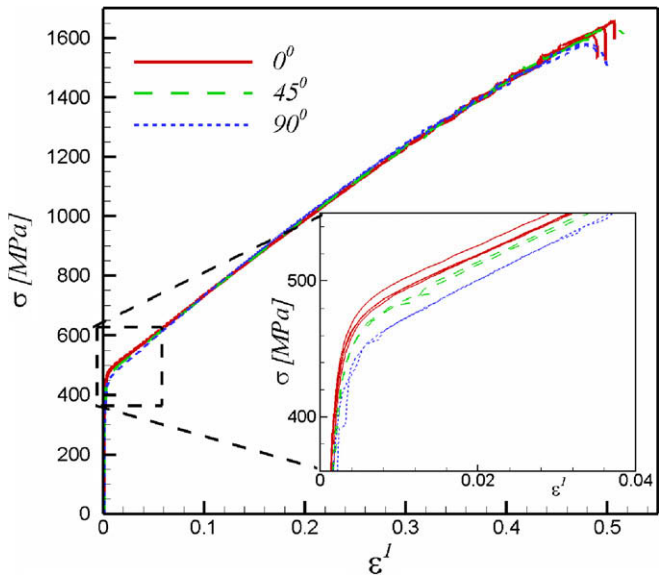
Fig. 4. True stress–true strain (ε^1, Eq. (2)) curves for specimens tested at a cross-head speed of 13 μm/s. Shown are results for 3–0°, 2–45°, and 2–90° specimens. The inset shows that the initial yield stress is affected somewhat by the specimen orientation (see Table 2).

the camera/specimen distance increases slightly during elastic deformation. In this case, the corresponding Young's modulus is unrealistically large. Alternatively, measured elastic strains that are too large result when the camera/specimen distance decreases slightly during elastic deformation, with the predicted Young's modulus then being unrealistically small. The true elastic strains, and, sub-

Table 2
Tensile properties of TWIP steel.

Tensile Specimen Orientation Relative to the Rolling Direction	Young's Modulus (GPa)	0.1% Offset Yield Stress (MPa)	0.2% Offset Yield Stress (MPa)	True Strain at the UTS From ε^1 Eq. (1)	UTS (MPa)	Maximum True Strain From ε^5 Eq. (4)	True Stress at UTS (MPa)
0°	195.8 ± 26	428 ± 15	454 ± 11	0.501 ± 0.007	1570 ± 22	0.648 ± 0.007	1683 ± 37
45°	202 ± 22	403 ± 3	440 ± 6	0.504 ± 0.002	1526 ± 23	0.770 ± 0.000	1707 ± 23
90°	189 ± 21	392 ± 6	425 ± 1	0.465 ± 0.005	1516 ± 35	0.798[a]	1611[a]

[a] These values were obtained from a single 90° specimen.

sequently, the Young's modulus can be more accurately determined by removing the errors from the "apparent" elastic strains. The Appendix details the steps taken to quantify the "apparent" elastic strains and remove the errors associated with them using DIC analysis. This procedure resulted in the Young's modulus values in Table 2. Note that errors in the elastic strains do not affect plastic strains.

3.2. Young's modulus variation with true strain

The Young's modulus of TRIP steels has been found to vary with strain in cyclic loading–unloading tensile tests (Doege et al., 2002; Hoanga et al., 2008). This behavior was attributed to "microplastic strains" associated with displacements of mobile dislocations and dislocation line geometry during inelastic deformation (Perez et al., 2005). Microplastic strains during unloading result from the "backwards" movement of dislocations from regions of dislocation "pile-ups" (Cleveland and Ghosh, 2002). Whether such mechanisms are active in high Mn TWIP steels is unknown and additional investigation of this issue will be necessary. Young's modulus behavior during elastic unloading at increased plastic strains is important for springback prediction in steel sheet stamping (Perez et al., 2005).

A series of loading–unloading tests on TWIP specimens cut at a 0° orientation relative to the rolling direction was conducted to investigate Young's modulus dependence on prior plastic strain. A substantial amount of data analysis was required since 1200–1300 digital images were recorded during each test and subsequently post-processed with the DIC algorithm. Each unloading period was terminated at a true stress ranging from 100 to 125 MPa so as not to risk termination of the image capture process and to avoid buckling. A small degree of hysteresis was noted between individual loading–unloading cycles. The extent to which twinning plays a role in the observed hysteresis, the amount of thermal energy dissipation, and the impact of other microstructural effects is unknown.

The single-sided technique for Young's modulus measurement detailed in Appendix A could not be used to compute Young's modulus values from the loading–unloading test results beyond the elastic stage. The reason for this is that that strain correction derived from initial loading cannot be applied to subsequent loading–unloading cycles. This required a second (and more instrumentation-intensive) measurement technique (detailed in Tong et al., 2008) in which both surfaces of a tensile specimen were simultaneously imaged with a dual mirror system. The mirrors were set at 45° to each surface with the camera positioned to look along the thinnest dimension of the specimen. Each surface therefore provided a set of Young's modulus and strain values for each loading and unloading step. Fig. 5 shows the variation of Young's modulus with strain from a representative test of a specimen with 0° orientation. This involved four loading–unloading steps beyond the initial loading step. Each data point resulted from averaging the computed stresses and strains from both surfaces of the tensile specimen during loading. For each cycle, the Young's modulus was fit to 80% of the peak reloading stress. The slope of each segment was then determined by linear regression. The trends shown in the two curves in Fig. 5 are representative of results from 0° specimens. A cubic polynomial, $E(\varepsilon^1) = c_1 + c_2\varepsilon^1 + c_3(\varepsilon^1)^2 + c_4(\varepsilon^1)^3$ was fit to the two data sets. Polynomial coefficients, c_i, as well as R^2 (goodness of fit) are listed in Table 3. Young's modulus under unloading decreases faster than that due to loading beyond ∼0.085 true strain.

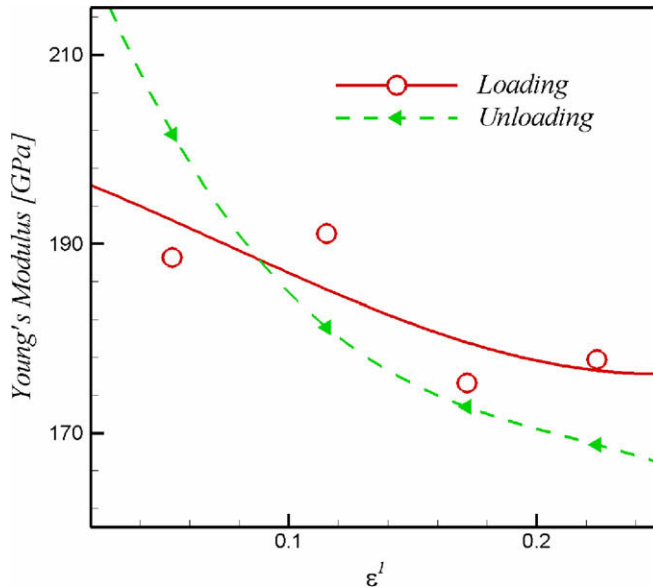**Fig. 5.** Young's modulus vs. true strain (ε^1, Eq. (2)) from DIC analysis of a periodic loading–unloading test of a straight gage tensile specimen with 0° orientation. A cubic polynomial was used to fit both the loading data (red solid line) and the unloading data (dashed green curve). For each cycle, the Young's modulus was fit to 80% of the peak reloading stress. (For interpretation of the references to color in this figure legend, the reader is referred to the web version of this article.)

Table 3
Cubic polynomial coefficients (c_i) in GPa and goodness of fit (R^2) from fits of $E(\varepsilon^1) = c_1 + c_2\varepsilon^1 + c_3(\varepsilon^1)^2 + c_4(\varepsilon^1)^3$ to loading–unloading data in Fig. 5.

	Loading	Unloading
c_1	198.294	233.734
c_2	−98.435	−760.456
c_3	−285.047	3217.403
c_4	1306.539	−4986.818
R^2	0.81	1.00

3.3. TWIP gage section thinning

At long times (e.g., 600 s and beyond), the S vs. e curves in Fig. 2 show small "humps" or serrations in what is otherwise a smooth variation of the load with time. The morphology of these serrations is dramatically different than the saw-tooth serrations commonly observed in Al–Mg alloys (e.g., AA5052-H32 in Tong et al., 2005a). Alternatively, the true stress–true strain curves in Fig. 3 (using ε^1 and ε^5 from Eqs. (2) and (3), respectively) display a step-wise behavior just beyond 0.3 true strain. As we shall demonstrate, this behavior is indicative of localized plasticity associated with Type A PLC bands. For the present TWIP material, these bands first nucleate over a short period of time, and then propagate across the gage section. Digital movies of TWIP tensile tests revealed a wave-like motion running back and forth along the tensile axis concurrent with a gradual thinning of the gage section width as tensile strain increased. No evidence of diffuse or localized necking appeared until a substantial elongation of each specimen had been attained.

Time-sequential deformation of a TWIP specimen as inferred from DIC analyses is shown schematically in Fig. 6. The black horizontal arrows denote the tensile load along the x-direction with the initial geometry shown in Fig. 6a. Note that the vertical scale in each figure has been exaggerated for the
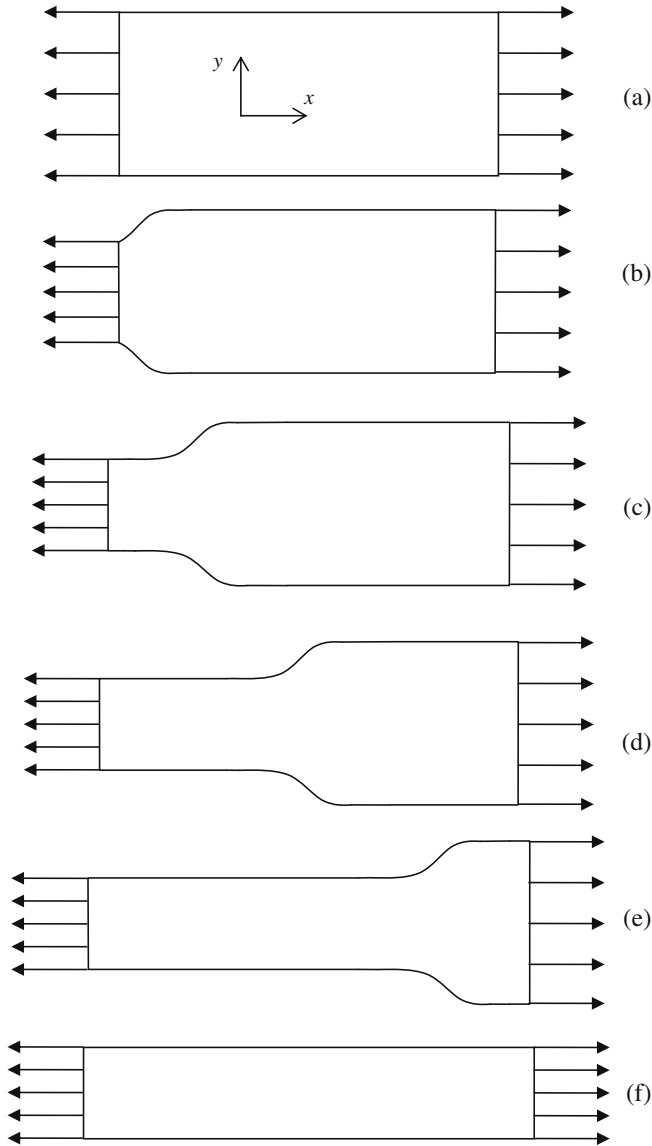
Fig. 6. Schematics of gage width thinning during PLC band propagation. For illustration purposes, displacements through the specimen width (along y) are exaggerated to emphasize local deformation. Arrows denote the tensile load. The undeformed gage section is shown in (a). A band enters the left end of the gage section in (b) which corresponds to the tapered region. A progressive reduction in the gage width occurs as the band propagates from left to right as shown in (c–e). A uniform reduction in the gage section width after the band exits to the right is shown in (f).

purpose of illustration. Fig. 6b shows a transition in the gage section geometry between thinned material and material that has not thinned. Uniform thinning continues with an additional increment as shown in Fig. 6c without diffuse neck formation as the region over which the abrupt change in width propagates to the right. Thinning of the gage section width continues in a left to right movement as shown in Fig. 6d and e as the tensile load increases. Finally, the gage section width in Fig. 6f, is uniformly narrower than in Fig. 6a. These small changes in the tensile specimen geometry are due to

the propagation of a single PLC band with increased plastic strain, which, in the case considered in Fig. 6, originates from the left end of the gage section. Propagation of subsequent bands continues to narrow the gage section width with no diffuse necking until just prior to fracture.

3.4. PLC effect in straight gage geometry with 0° orientation

3.4.1. Band nucleation and propagation

Direct measurement of band nucleation and propagation was obtained from contour maps of true strain and true strain rate computed with the DIC algorithm. Unless otherwise specified, contour maps are displayed in the undeformed system since necking did not occur until much later in the tensile tests. Contours of constant axial true strain rate, $\dot{\varepsilon}$ (1/s), were computed by dividing the incremental true strains with the time step between the associated sequential images using a backward differentiation scheme where $\dot{\varepsilon}_t = \Delta\varepsilon/\Delta t = (\varepsilon_t - \varepsilon_{t-1})/\Delta t$.

Fig. 7a, c, e, and g are DIC-computed strain rate contour maps that show the nucleation of a single Type A PLC band near the center of a 0° straight gage tensile specimen with increasing strain. Note that contour values of $\dot{\varepsilon}$ are listed in the key in Fig. 7i. Fig. 7e and g show that the band actually consists of crossing shear bands at ±54° angles relative to the tensile axis which runs along the horizontal of each map. This angle is close to the 53.1° measurement reported in Chen et al. (2007) using infrared thermography. A peak strain rate of 0.005 1/s is denoted by the red contour patches in the band shown in Fig. 7g. We note that the level of detail associated with the strain rate contour map containing the crossing shear bands was not observed in all tests since the extent of the central (red) contour patch typically spanned the entire width of the gage section. A wider tensile specimen may in fact be required in order to consistently image the crossing shear bands shown in Fig. 7g. Fig. 7b, d, f and h show corresponding contours of true axial (cumulative) strains, ε, resulting from DIC analysis of tensile specimen images captured at t = 723, 726, 727, and 729 s, and the initial image of the undeformed specimen surface. Contour values of ε from the DIC analysis are listed in Fig. 7j key. Note that blue strain contours in Fig. 7b, d, f, and h appear mostly to the right of the band as it nucleates in Fig. 7c, e, and g. These blue contours correspond to the smallest true strain value of 0.4 in Fig. 7j.

Following the nucleation process in Fig. 7, band propagation starts in Fig. 8a, and proceeds to the right of center of the gage section, as shown in Fig. 8c, e, and g. Interestingly, the blue contour patches in Fig. 7b, d, f, h, and j are indicative of the direction of band propagation following nucleation. The PLC band propagation is responsible for the wave-like motion observed in digital movies of straight gage tensile specimens alluded to earlier. The orange-red true strain contours which increase in lateral extent from Fig. 8d to Fig. 8g to Fig. 8h show that plastic strains accumulate in the wake of the propagating band. Infrared thermography from Chen et al. (2007) suggests that the orange-red contours correspond to material that has been heated during band propagation. Note that the gage section width has decreased between Fig. 8a and g following the schematics in Fig. 6. For this particular case (depicted in Figs. 7 and 8), Δt is approximately 3 s. Given the band speed of 0.41 mm/s, this gives incremental steps of $\Delta x \approx 1.23$ mm which is significantly less than the band width of ~5 mm (i.e., along the horizontal or tensile axis).

It has previously been suggested that band nucleation occurs at the gripper ends (Chen et al., 2007) due to geometric non-uniformities. However, the behavior shown in Fig. 7a, c, e, and g tends to suggest otherwise. Although the tensile specimen from which the results in Figs. 7 and 8 were generated had no taper, the location of band nucleation close to the center of its gage section prompted a more thorough investigation of fracture surfaces and a possible role of inclusions. Common to most of the fracture surfaces analyzed were sporadic inclusions (approximately 2 for each 100 μm^2 SEM image) with diameters ranging from 2 to 5 μm. Each was surrounded by larger voids. Energy dispersive spectroscopy (EDS), which has previously been used to investigate inclusion morphology and chemistry in fracture surfaces of press-hardened boron and fully martensitic steels (Savic and Hector, 2007; Savic et al. 2008), revealed high levels of Al and S along with Ca, Mn, Ti, Si, and Fe. No reasonable link between inclusions and the location of band nucleation could be established and the underlying causes of the band nucleation position in Fig. 7a, c, e, and g may be related to material heterogeneities, e.g., texture.
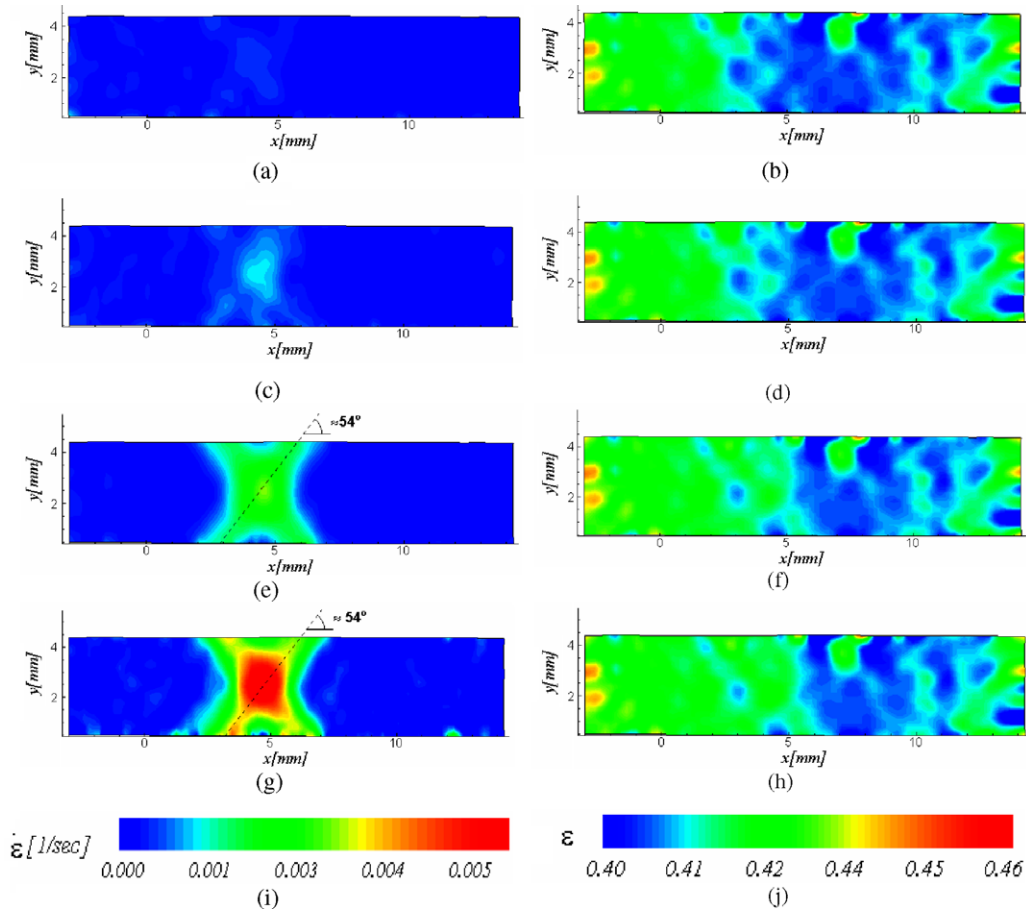
Fig. 7. Nucleation of Type A PLC bands near the center of a straight gage TWIP specimen as computed from DIC shown in the deformed configuration. Incremental true strain rate contours (at increasing times) are shown in (a), (c), (e), and (g). Corresponding cumulative true strain contours are shown in (b), (d), (f), and (h). Time durations following the start of the test were 723 s (b), 726 s (d), 727 s (f), and 729 s (h). The contour keys in (i) and (j) show that red contours correspond to peak strain rates in the incremental maps, and peak true strains in the cumulative maps. Tensile loads associated with (b), (d), (f), and (h) were 7210, 7232, 7221, and 7209 N, respectively. Load increments associated with the incremental strain rate contour maps range from ΔF = 12 to 22 N. (For interpretation of the references to color in this figure legend, the reader is referred to the web version of this article.)

3.4.2. DIC analysis of serrations

Band propagation in TWIP and other austenitic steels reported in previous work was not thoroughly explored in the vicinity of serrations in load–time records and true stress–true strain curves (Chen et al., 2007; De Cooman et al., 2008; Cuddy and Leslie, 1972; Pink and Kumar, 1995; Cunningham, 1999; Mannan et al., 1983; Chan et al., 1997). The DASYLab image acquisition algorithm, combined with the high speed digital camera, and DIC algorithm used in the present investigation enabled careful study of band propagation at any point in the tests where the bands appeared.

Fig. 9a shows a typical load–time profile at long testing times. Each "hump" or serration (denoted by labels A, B, C, D, and E in the plot) occured at intervals of approximately 80 s in this test. Images were taken at approximately 3.8 s intervals giving a total of 64 images over the time period shown in Fig. 9a. The peak force levels associated with the five serrations, which fall on the dashed vertical lines, appear to grow with increasing time only to significantly diminish just before fracture. Fig. 9b
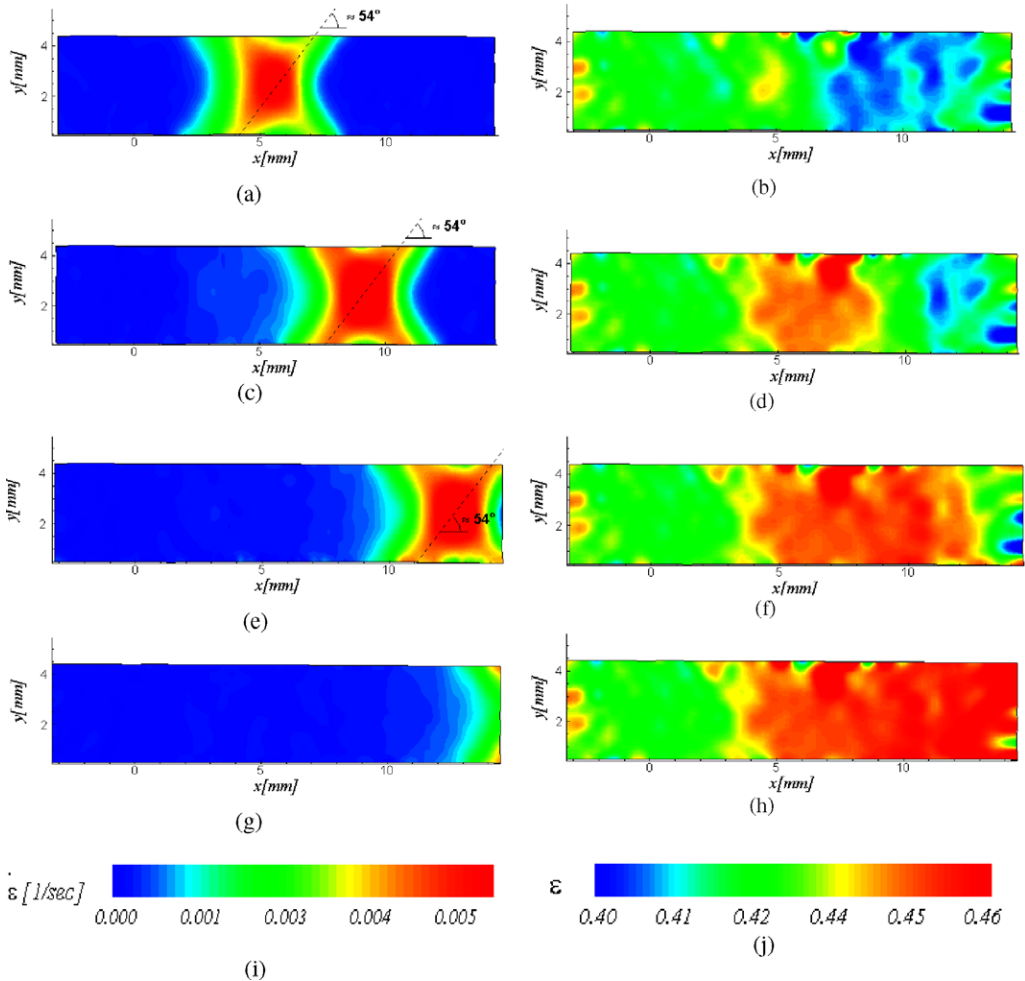
Fig. 8. Propagation of Type A PLC bands following nucleation process detailed in Fig. 7 (also, in the deformed configuration). Incremental true strain rate contours at increasing times are shown in (a), (c), (e), and (g). Corresponding cumulative true strain contours are shown in (b), (d), (f), and (h). Time durations following the start of the test are 732 s (b), 738 s (d), 744 s (d), and 750 s (h). Red contours denote peak strain rates in the incremental maps, and peak true strains in the cumulative maps. The contour keys in (i) and (j) show that red contours correspond to peak strain rates in the incremental maps, and peak true strains in the cumulative maps, respectively. The loads in (b), (d), (f), and (h) are F = 7199, 7202, 7207, and 7211 N, respectively. The increments associated with the incremental strain rate contour maps range from ΔF = 3 to 5 N. (For interpretation of the references to color in this figure legend, the reader is referred to the web version of this article.)

shows a single serration from a special test in which the camera was triggered only during the time when the serration appeared in the load-time record. Here, the open circles superimposed on the curve appear at times at which single images were captured with the variable rate image acquisition algorithm. Image capture for this single serration was at 0.2 s intervals.

Fig. 10a is an enlarged view of the engineering stress–engineering strain (S and e) curve in Fig. 3 showing step-like serrations. The regions between serrations A and B and B and C show a linear increase in stress, while the regions between serrations C and D and D and E are at a nearly constant stress. It is because of the linear increase in the flow stress (as shown in the regions between serrations A and B and B and C in Fig. 10a) that Chen et al. (2007) refer to the associated bands as "modified" Type
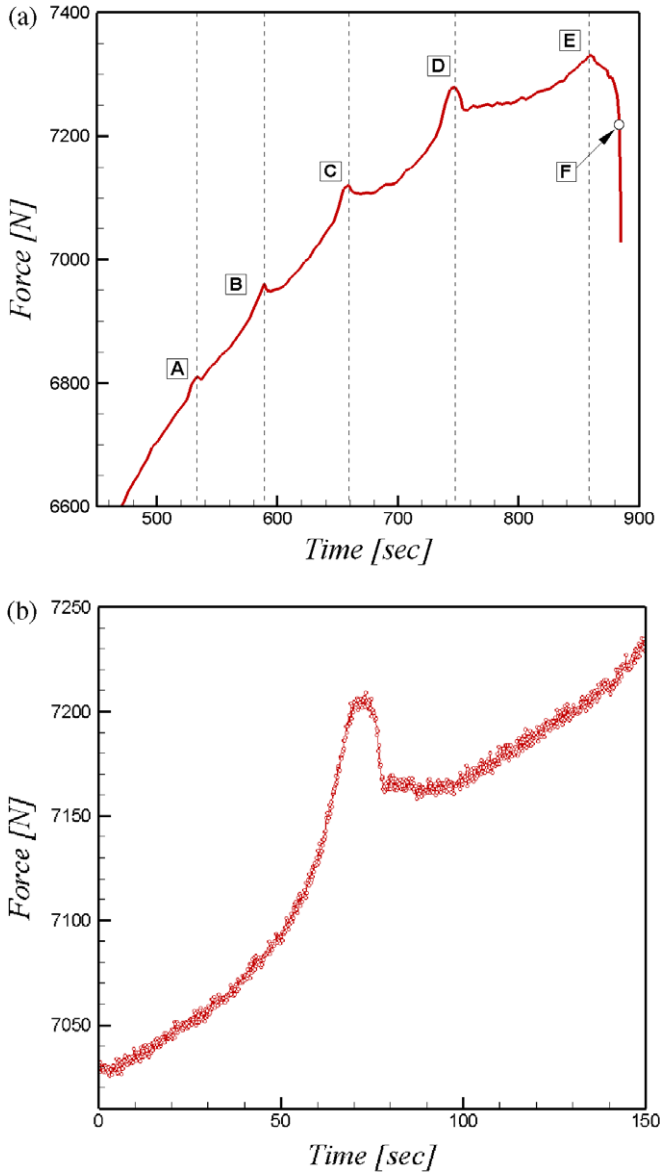
Fig. 9. (a) Enlarged view of a typical load–time record showing humps or serrations that appear at long times. The last serration (i.e., just before 900 s) is followed by localized necking and fracture. (b) Details of one of the serrations taken from a special test with a 5 image/s capture rate. Captured images are denoted by the open circles superimposed on the curve.

A PLC bands (i.e., the stress does not achieve a constant value between all serrations). This is also shown in Fig. 2a of Chen et al. (2007) and it is indicative of local strain hardening of material due to a PLC band. Chen et al. (2007) also point out that the "modified" Type A PLC bands bear some resemblance to Lüders bands in low carbon steels. Stress–strain curves are typically flat during Lüders band propagation as is the case for the regions between serrations C and D and D and E in Fig. 10a. Also note the apparent yield point phenomenon denoted by the "spike" in the engineering stress at D (and to a lesser extent at E). The high frequency oscillations at the highest strains which Chen et al. (2007)
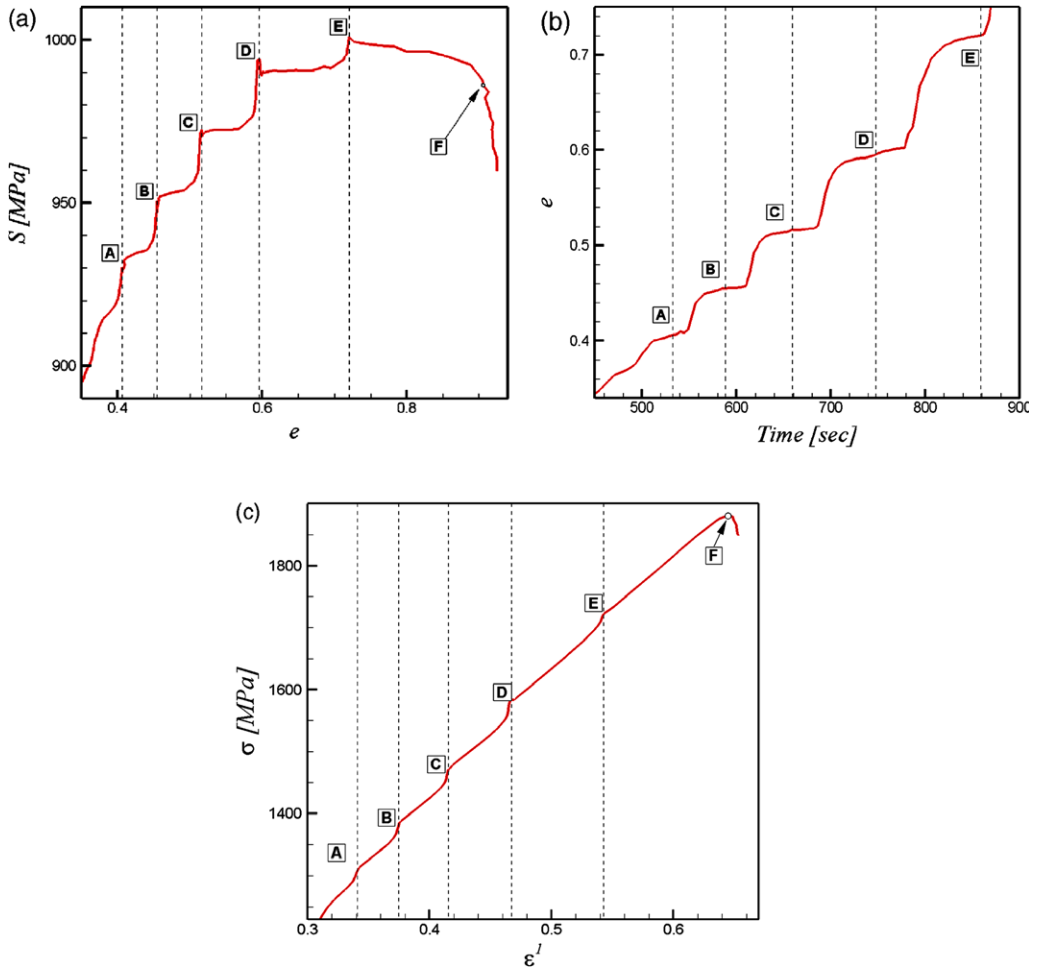
Fig. 10. Enlarged views of the (a) S vs. e in Fig. 3, (b) e vs. time over the same time period as in (a), and (c) the DIC-computed true stress–true strain (ε^1, Eq. (2)) curve in Fig. 3 showing the step-increments beyond 0.3 true strain. Five serrations labeled as A–E appear, with the peak true stress noted at F. Oscillations at the highest strains which correspond to the Type B (or C) PLC bands observed in Chen et al. (2007) and Allain et al. (2008) do not appear.

referred to as Type B PLC bands do not appear in this plot and in fact they were not observed in any of our stress–strain plots. It is possible, however, that the bands observed at the largest strains in Chen et al. (2007) were Type C. Differences in the specimen geometries and/or TWIP chemistries with those in the present study and those in Chen et al. (2007) may have influenced the PLC band types observed in both studies. Fig. 10b shows the evolution of the engineering strain, e, over the same time period considered in Fig. 10a. Note that the step-like behavior is qualitatively similar to Fig. 2b of Chen et al. (2007). Fig. 10c shows the DIC-computed true stress–true strain (ε^1, Eq. (2)) curve in Fig. 3. The serrations first appear beyond a 0.3 true strain and intermittently appear through 0.54 true strain.

Fig. 11 is a more thorough examination of the spatio-temporal characteristics associated with band nucleation at, and propagation, from the left gripper end of TWIP tensile specimen. This is the behavior that is commonly cited in the PLC literature. The load–time record which is the red curve on the left (i.e., Force vs. Time) of Fig. 11 covers a portion of the total testing time: this shows three serrations. The axial true stress–true strain (ε^1, Eq. (2)) is shown on the right. Between the two plots (i.e., running
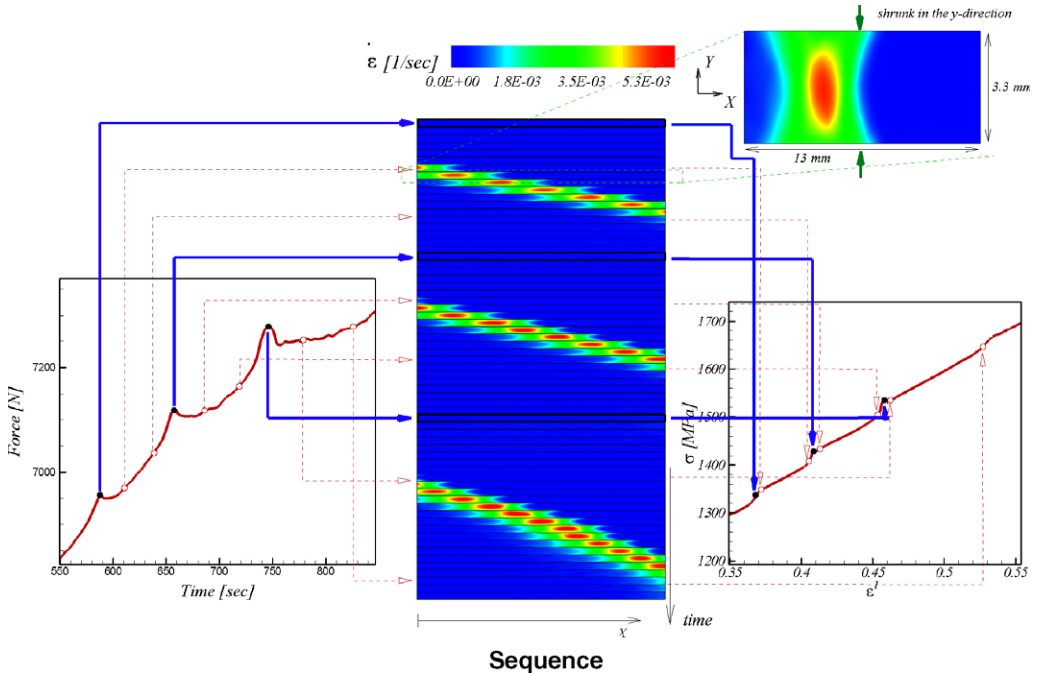
Fig. 11. Spatio-temporal behavior of the Type A PLC band in a straight gage section test with a 0° orientation where the bands nucleated at (or near) the left gripper end. The load–time record is shown on the left and the DIC-computed true stress–true strain (ε^1, Eq. (2)) curve is shown on the right. The sequence of strain rate contour maps at the center denotes the propagation of three distinct bands from left to right across the gage section area (rectangular boundary of each contour map) during a tensile test. Each contour map (plotted in the undeformed configuration) in the sequence has been shrunk from its original size which is shown in the full-size contour map at the upper right of the figure (labeled "shrunk in the y-direction"). Peak strain rates of 5.3×10^{-3} 1/s are indicated by the red contour patches. Solid blue lines connect the peaks of the "serrations" in the load–time record with the step-like profile in the true stress–true strain plot. Band propagation occurs at times denoted by the two open red circles that fall between each serration (step) in the load–time (true stress–true strain) curves. (For interpretation of the references to color in this figure legend, the reader is referred to the web version of this article.)

down the center of Fig. 11) is a sequence of strain rate contour maps from DIC analysis. These maps are stacked one on top of the other to show the propagation of three PLC bands moving from left to right across the gage section (along the x-axis or gage length as indicated beneath the sequence). Note that time increases from the uppermost to the lowermost of these strain rate contour maps (i.e., from top to bottom) as indicated by the arrow at the lower right of the sequence. For illustration purposes, each contour map in the sequence is compressed along the y-direction with the center of each corresponding to the center of the gage section. The original shape (13 mm × 3.3 mm) of each contour map in the sequence is shown at the upper right. Note that the green arrows indicate how the map was shrunk to fully display PLC band propagation in the sequence. The band propagation events occur in just under 300 s (i.e., following the time axis in the load–time record to the left of the sequence). The strain rate contour key at the top of the sequence shows a peak value of the strain rate (red contour patch) of 5.3×10^{-3} 1/s. The circles superimposed on the red curve in the load–time plot denote important events associated with band propagation as quantified in the strain rate contour sequence. The solid black circles are placed at the peak of each hump or serration in the load–time record. A blue solid line emanates from each black circle with an arrow at its other end pointing to one of the strain rate contour maps in the sequence. For example, the blue line that emanates from the circle at 587 s (6960 N) in the load–time record points to the uppermost contour map which is entirely blue since no band has appeared at this stage of deformation. This strain rate map was computed from incremental correlation of images just before and after 587 s into the test. Specific points at which images were recorded

are not shown in either plot for the sake of clarity. Hence, the time corresponding to each circle is the average time between two successive digital images recorded from the tensile specimen surface. Each contour map in the sequence that is associated with a peak in each serration in the load–time plot is bounded by thick black borders to distinguish it from other maps. Two open red circles have been placed between successive black circles in the load–time record. From each of these emanates a red dashed line with an arrow at its end that points to a specific contour map in the sequence. The red open circles that fall 20–30 s beyond each black circle are positioned at those times at which a band enters "the window" of a contour map from the left end. The red circles that fall 60–100 s beyond each black circle are positioned at those times where a band has just exited a strain rate contour map. For example, the first red open circle in the load–time record falls just beyond 610 s (6970 N). The red dashed line that emanates from this red circle leads to an incremental strain rate map (seventh from the top of the sequence) with a small region of colored contours at its left end (topmost dashed horizontal line with a red arrow). These contours denote strain rates associated with a band entering the field of this contour map at this time. The seven maps that follow beneath this map show this band propagating across the gage section at times corresponding to the open circles between the peaks of the first two serrations in the load–time record. The second open red circle that falls at 640 s (second dashed horizontal line with a red arrow from the top) denotes the point at which the band has exited the 13 mm × 3.3 mm gage section area. Once the peak of the second serration appears in the load–time plot at 660 s (7120 N), no band propagation occurs as indicated by the solid arrow that points to the second DIC map surrounded by a black border. Beyond the second serration, a band appears once again at 685 s (7116 N) from the left end. The process repeats a third time beyond the third serration at 743 s (7275 N) in the load–time record. The specimen rapidly necks and fractures just beyond the fourth serration in the load–time record (not shown). Fig. 11 shows that band propagation occurs between the peak loads associated in the load–time record. The peak loads correspond to nucleation events at or near the left gripper which are not shown in the sequence.

Peaks in the serrations of the load–time record correspond to graded "steps" in the true stress–true strain curve (where the uniaxial strain measure in Eq. (2) is used). This is shown in the plot to the right of the sequence in Fig. 11. The dark blue lines that emanate from serrations in the load–time record continue to the right of the sequence and point to solid black circles in the true stress–true strain plot. Each of these circles falls at the top of a graded step at which point band propagation is not observed in the corresponding contour maps of the sequence (i.e., those with the dark borders). Each red dashed line that emanates from an open red circle in the load–time record is also continued to the right of the sequence, and points to open red circles superimposed on the true stress–true strain plot. For example, the two open red circles between 0.37 and 0.405 true strain correspond to the first and second open red circles in the load–time record at 610 and 640 s, respectively. Hence, band propagation occurs between the steps in the true stress–true strain plot.

Fig. 12 explores strain accumulation in the wake of the third propagating band (i.e., between 782 and 822 s) in Fig. 11. Fig. 12a and b are representative true axial strain rate and strain contour maps, respectively, at 806 s. Each has a superimposed black dotted line positioned along its center at $y = y_0 = 2$ mm. It is along this line that profiles of both the true strain (red) and true strain rate (blue dashed) are plotted in Fig. 12c–h (at 8 s increments) to explore how the local strain changes during Type A PLC band propagation. For example, the blue dashed curve in Fig. 12c, which resembles a wave, is strain rate with position across the gage section and corresponds to the band entering the window at 782 s (see the second dashed red arrow from the bottom of the sequence in Fig. 11). This curve moves from left to right in Fig. 12d–h with a very small decrease in the peak strain rate from 0.0061 1/s in Fig. 12c to 0.0058 1/s in Fig. 12h. In Fig. 12b–h, the red curve shows that strains immediately behind the band increase as the band moves across the gage length. This is consistent with changes observed in the extent of the orange-red contours in Fig. 7d, f, and h. In Fig. 12h, the band exits the window but leaves strained material in its wake.

Fig. 13a shows the spatial evolution of cumulative axial strain from DIC contours due to propagation of the three successive PLC bands in Fig. 11 over the same length of gage section. A family of selected curves is shown for each of the three bands. For example, the red curves associated with band 3 correspond to contours in the sequence in Fig. 11 that span the time period ranging from 770 to 827 s, along with additional curves at both smaller and larger strains just outside of the time frame of band 3.
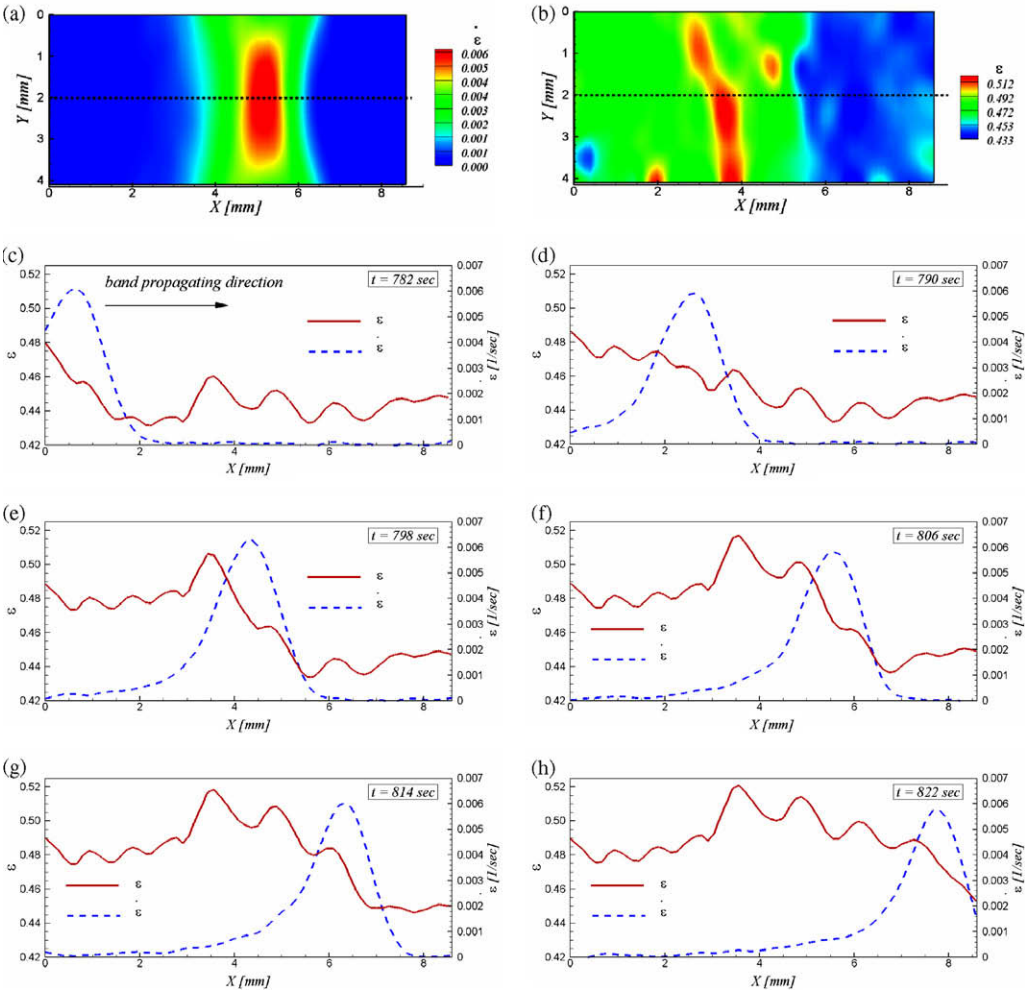
Fig. 12. Two-dimensional profiles through contours of true axial strain (solid red curves) and incremental strain rate (dashed blue curves) with position across the gage section. These correspond to the third propagating band event (i.e., at the longest time) in Fig. 11. Shown at the top are representative strain rate and strain contour maps (in the undeformed configuration) at 806 s with superimposed black dotted horizontal lines at $y_0 \sim 2$ mm denoting the path along which the profiles in (c–h) are generated. Cumulative true axial strain $\varepsilon = \varepsilon(X, Y_o)$ and incremental strain rate $\dot{\varepsilon} = \dot{\varepsilon}(X, Y_o)$ are taken from DIC-computed contour maps. Band movement, which is left to right, is shown by the blue strain rate curves in (c–h) while true strain profiles are red. (c) Band entrance at 782 s ($\varepsilon^1 = 0.46$); (d) 790 s ($\varepsilon^1 = 0.465$); (e) 798 s ($\varepsilon^1 = 0.47$); (f) 806 s ($\varepsilon^1 = 0.47(5)$); (g) 814 s ($\varepsilon^1 = 0.48$); (h) band exit at 822 s ($\varepsilon^1 = 0.48(4)$). Note the increase in strain between (c) and (e) behind the blue curves in these figures. (For interpretation of the references to color in this figure legend, the reader is referred to the web version of this article.)

Propagation of band 3 causes the strain to suddenly increase from point to point across the gage section as the curves spread apart. When the curves surrounding those corresponding to band 3 are bunched up, no propagation occurs. Similar observations apply for the earlier bands associated with the green and red curves in Fig. 13a. In Fig. 13b, cumulative strain, ε (red), and incremental strain rate, $\dot{\varepsilon}$ (dashed green), from DIC-computed contour maps along the dashed vertical line at $X = 3.9$ mm in Fig. 13a are plotted. The blue dashed curve shows the load–time profile from Fig. 11 which is included for reference. The cumulative axial strain from the DIC contours, ε, follows a stepped profile as the bands pass through $X = 3.9$ mm. Alternatively, the strain rate profile is a series of discrete "spikes" each
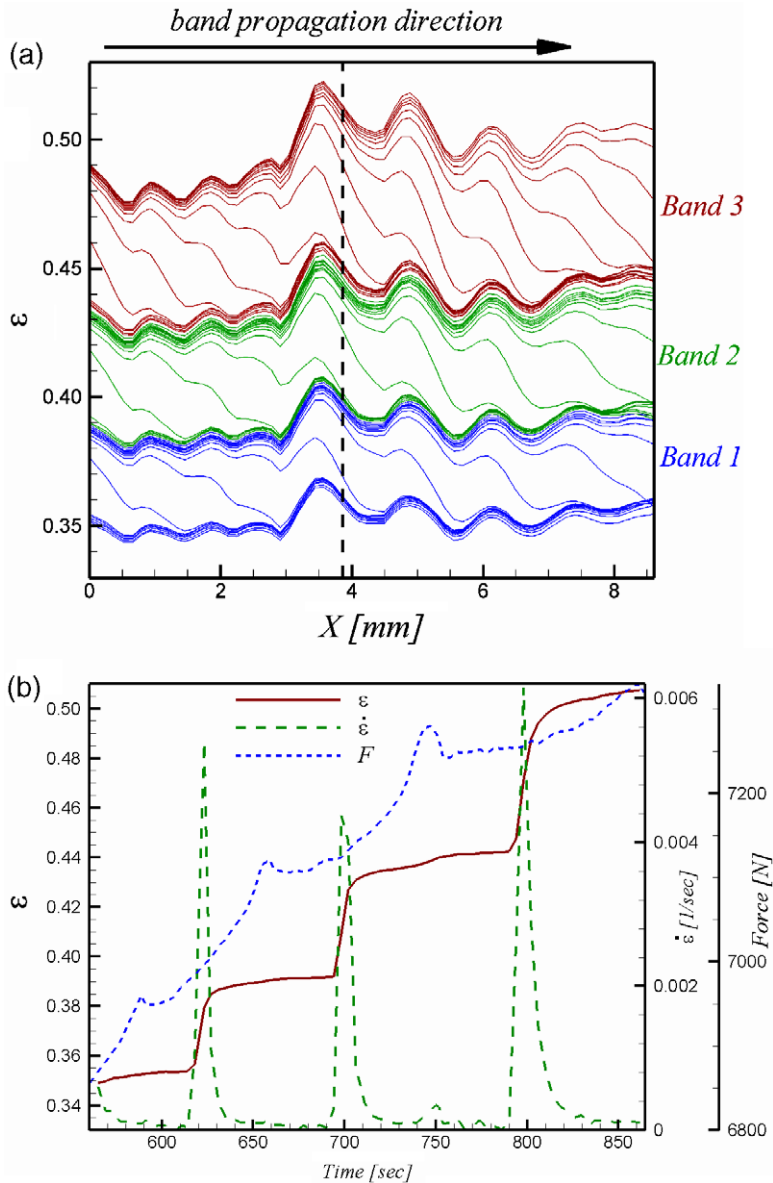
Fig. 13. (a) Spatial variation of cumulative axial true strain ε as three PLC bands pass through the same length of gage section. Here X corresponds to the undeformed configuration. Strain profiles associated with each of the three bands are labeled accordingly. (b) Evolution of ε (red) at $X = 3.9$ mm (i.e., at the position denoted by the dashed vertical line in (a)) follows a step profile, while that of the incremental true strain rate $\dot{\varepsilon}$ (green) is localized into "spikes" which denote passage of the band at $X = 3.9$ mm. The load–time record is shown in blue. Cumulative true axial strain and incremental strain rate are taken from DIC-computed contour maps. (For interpretation of the references to color in this figure legend, the reader is referred to the web version of this article.)

of which falls between serrations in the load–time profile, as expected. The peak strain rate is concurrent with the mid-point of the strain serration and fluctuates between 0.0048 and 0.0055 1/s. Once the band passes through $X = 3.9$ mm, the axial strain increases only slightly up to the point where the next band appears while $\dot{\varepsilon}$ falls to a nearly constant value.

We further explore band nucleation and propagation from the gage section center previously considered in Figs. 7 and 8. Additional bands nucleated (one at a time) near the center of the gage section in this test and then propagated in either direction shown in Fig. 8 (i.e., center-to-right) or opposite to it. Fig. 14 explores this behavior in greater detail following the format of Fig. 11 from yet another tensile test where band nucleation occurred near the center of the gage section. Three band nucleation and propagation events are shown in Fig. 14, over a 340 s time frame, in the sequence of true strain rate contour maps at the center of the figure. A time axis is included to the right of the sequence. The first and third bands propagate to the left (as indicated by the positions of the red contour patches) and the second band propagates to the right of the tensile specimen. Two load–time records (which are part of the same overall time record) are shown to the left of the strain rate contour sequence, with the plot at the top left showing two serrations over a 110 s time frame, and that below it showing two subsequent serrations that appear with additional tensile strain over the next 110 s. Corresponding true stress–true strain (ε^1, Eq. (2)) plots are shown to the right of the sequence. Red contours in the contour key at the top of the sequence denote a peak strain rate of 0.0021 1/s. Solid circles are positioned at the peaks of the serrations in the load–time plots. Arrows at the end of the blue lines emanating from these circles point to contour maps in the sequence that signal the appearance of green-yellow contours: these denote band nucleation at positions near the center of the gage section. Band nucleation occurs at the peaks of the load–time serrations, as expected. Similarly, in the true stress–true strain profiles to the right of the sequence, band nucleation occurs at the peaks of the serrations. It is tempting to attribute band nucleation and propagation from a point near the center of the straight gage section to the lower strain rates depicted in Fig. 14. However, such
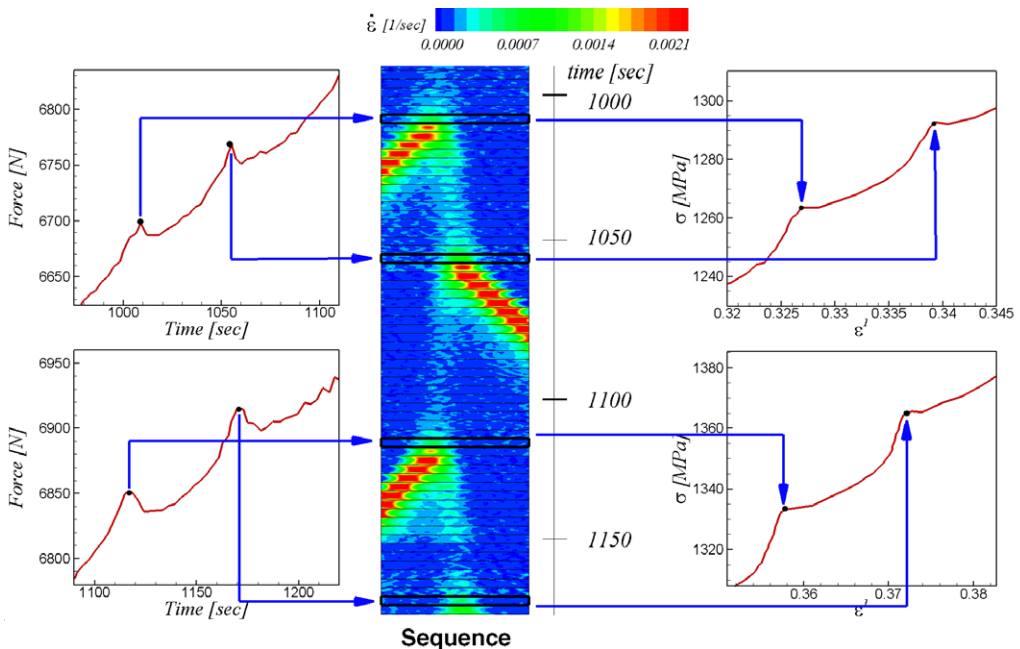

Fig. 14. Spatio-temporal behavior of the Type A PLC band in a straight gage section test with a 0° orientation where the bands nucleated near the center (rather than at one of the gripper ends) of the gage section. Strain contours corresponding to three bands are shown in detail with a fourth nucleating at the longest times shown. The frames with thicker borders correspond to peaks in the serrations of the load–time record (shown in two parts, with filled circles at the peaks of the serrations) at the left of the strain rate contour sequence. As expected, band nucleation occurs at the peaks of the serrations. The axial true stress–true strain plot to the right of the sequence (shown in two parts) suggests that band nucleation is concurrent with the highest points of each step. These are denoted by the filled circles to which point the blue arrows from the strain rate contour sequence. The horizontal length of each contour map in the sequence is 10 mm.

behavior was also observed at strain rates comparable to those associated with Fig. 11 and hence such a conclusion is erroneous.

Fig. 15 explores strain accumulation in the wake of a single band that preceded those shown in Fig. 14 (i.e., between 952 and 973 s into the test). The analysis is identical to that in Fig. 12. In this case, however, a period of band nucleation is followed by band propagation to the right of the gage section. Band nucleation is shown in Fig. 15a and b with the rise in the peak associated with the strain rate (blue dashed). At $t = 958$ s in Fig. 15c, the band begins to move to the right, with peak strain rates increasing in Fig. 15d and e, and then exits the window in Fig. 15f at $t = 973$ s. The red curve in each figure shows that as the band nucleates, the cumulative axial true strain increases as well.

The analysis in Fig. 16 for the spatial evolution of the cumulative true axial strain is identical to that in Fig. 13a. However, Fig. 16 explores the case where four PLC bands nucleate near the center of TWIP tensile specimen rather than at its left or right gripper end. Band nucleation occurs between 4 and 5 mm (i.e., near the center of the gage section). Bands 1 and 3 propagate to the left, bands 2 and 4 propagate to the right. The strain increases with the nucleation and propagation of each band, but does so non-uniformly along the gage length in contrast with the nearly uniform increase in strain shown in Fig. 13a. The strain profiles shown in Figs. 13a and Fig. 16 represent two spatio-temporal signatures of the TWIP steel deformation history due to band nucleation and propagation.

3.4.3. PLC band kinematics

The cumulative strain contour maps in Fig. 8d, f, and h show that strains increase in the wake of a propagating band. It is of interest to investigate whether the band speed reaches a steady state, and
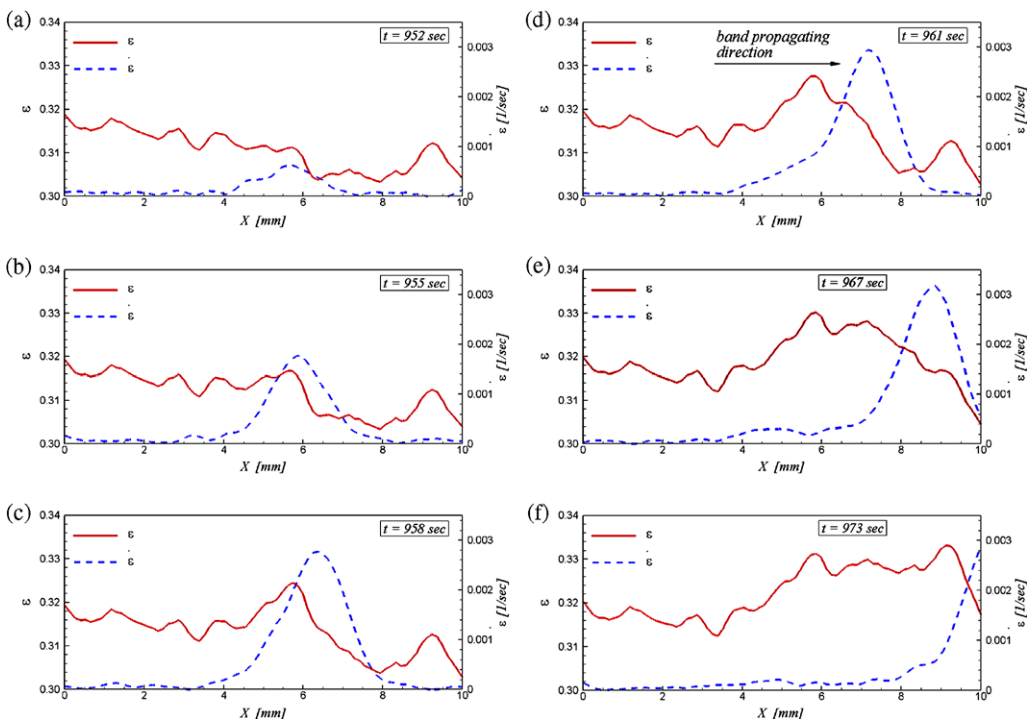

Fig. 15. Two-dimensional profiles through contours of cumulative true axial strain (solid red curves) and incremental strain rate (dashed blue curves) with position across the gage section corresponding to a time period preceding that of Fig. 14. Cumulative true axial strain $\varepsilon = \varepsilon(X,Y_o)$ and incremental strain rate $\dot{\varepsilon} = \dot{\varepsilon}(X,Y_o)$ are taken from DIC-computed contour maps. Band nucleation: (a) 952 s ($\varepsilon^1 = 0.31(3)$); (b) 955 s ($\varepsilon^1 = 0.31(4)$); (c) 958 s ($\varepsilon^1 = 0.31(5)$). Band propagation to the right: (d) 961 s ($\varepsilon^1 = 0.31(6)$); (e) 967 s ($\varepsilon^1 = 0.31(8)$), (f) 973 s ($\varepsilon^1 = 0.32$). (For interpretation of the references to color in this figure legend, the reader is referred to the web version of this article.)
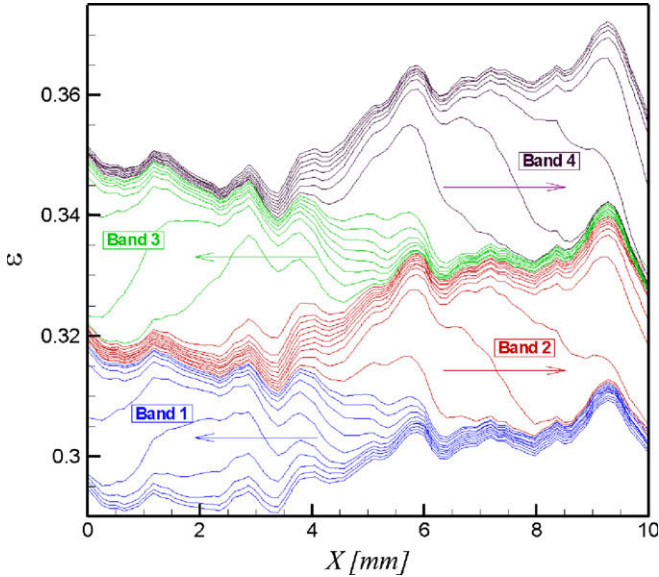
Fig. 16. Spatial variation of cumulative true axial strain ε as four PLC bands nucleate near, and propagate from the center of the gage section. Here X corresponds to the undeformed configuration. Strain profiles associated with each of the four bands are labeled accordingly. Nucleation of each band occurs between $X = 4$ and 5 mm. Bands 1 and 3 propagate to the left, bands 2 and 4 propagate to the right. No band nucleation and propagation occurs when the curves are closely spaced. Cumulative true axial strain is taken from DIC-computed contour maps.

the extent to which increasing strains in the band wakes impact the motion of subsequent bands. Fig. 17a shows the time variation of band travel distance Δx (mm) relative to the nucleation point near the center of the gage section (in the deformed configuration) as shown in the two inset figures. The red and blue curves correspond to separate tests at applied cross-head displacement rates of $\dot{\delta}_{App} = 7$ and 13 μm/s. Each point denotes the point of maximum strain rate in the corresponding strain rate contour maps. The applied strain and applied strain rate are defined as $\varepsilon_{App} = \log(L/L_0)$ and $\dot{\varepsilon}_{App} = d\varepsilon_{App}/dt$, where L_0 is initial gage length and $L = L_0 + \delta$ (with δ being the applied or cross-head displacement). As expected, the band in the test with the higher cross-head speed travels a greater distance in a comparable period of time compared with that in the slower 7 μm/s test. Fig. 17b relates the band speed, $v = dx/dt$ (in mm/s) relative to nucleation time for the same two tests. After (approximately) 10 s beyond nucleation, the band in the 7 mm/s test reaches a steady state at an average speed of 0.16 mm/s. Alternatively, the band in the 13 μm/s test accelerates over nearly twice the time as the 7 μm/s band reaching an average speed of 0.41 mm/s.

Fig. 18 shows the variation of $v/\dot{\delta}_{App}$ with ε_{App}. Data from two tests conducted at a 13 μm/s cross-head speed (open and solid red circles) and one at 7 mm/s (green triangles) are shown. The data points correspond to the peak strain rate (DIC-computed) contour values associated with many bands traveling across the gage sections as the applied strain, ε_{App}, is increased. We note that a linear trend in the data denoted by the dashed line suggests that the band strain increases with increasing applied strain. This makes sense from the standpoint that successive bands must pass through increasingly strained material which subsequently reduces their speeds. An analysis similar to that in Fig. 18 revealed that band speed (or band strain) is only very weakly dependent upon $\dot{\varepsilon}_{App}$. In addition, Figs. 10b and Fig 13a suggest that band strain increases with each band, and hence confirms Eq. (3) of Chen et al. (2007) in which $v/\dot{\delta}_{App} = 1/f(\varepsilon_b)$, where $f(\varepsilon_b)$ is an increasing function of the band strain, ε_b.

Fig. 19 shows the normalized steady-state peak band strain rate $\dot{\varepsilon}_{peak}^{st}/\dot{\varepsilon}_{App}$ with ε_{App} from three tensile tests. The peak band strain rate $\dot{\varepsilon}_{peak}$ is defined as the maximum strain rate value in the entire DIC window. When a band nucleates, $\dot{\varepsilon}_{peak}$ increases from zero up to $\dot{\varepsilon}_{peak}^{st}$, which is defined as the steady-state
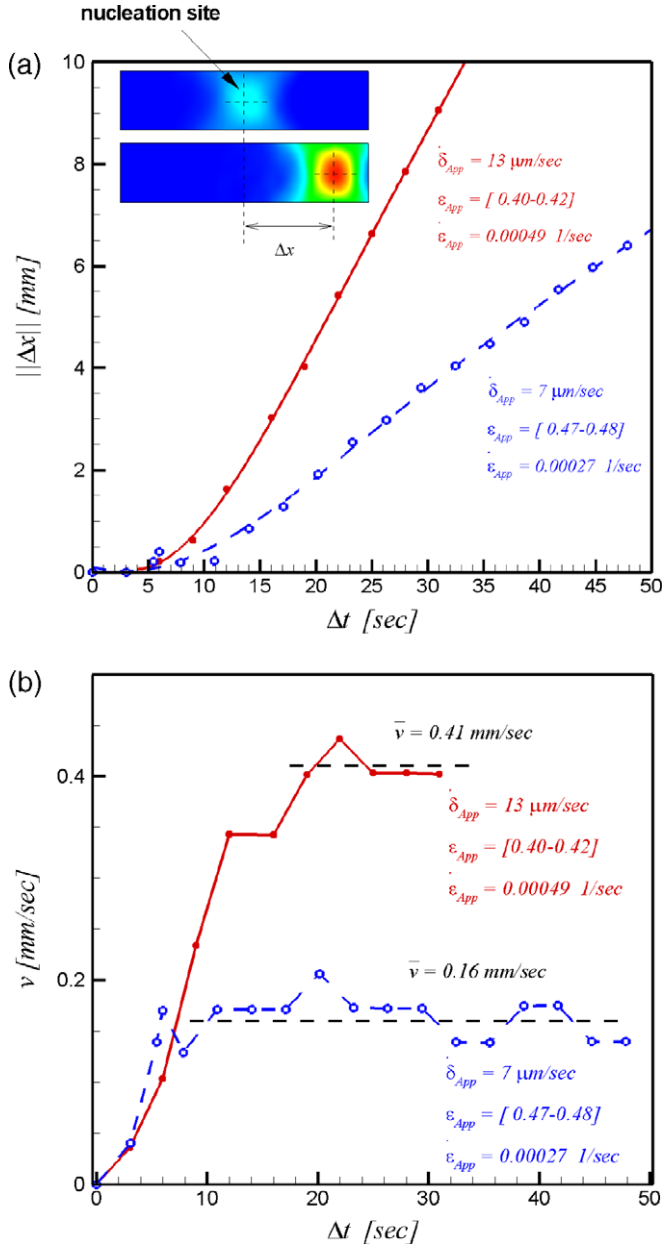
Fig. 17. (a) Travel distance Δx relative to the center of band nucleation vs. time for two representative cases. The case with lower applied displacement rate shows a slower band speed. (b) Band speed, $v = dx/dt$. After nucleation, the bands essentially reach a steady state during which they propagate at nearly a constant average speed through the gage length until exiting the DIC window. Distances and velocities are measured in the deformed configuration.

value. Each group of points (connected by dashed lines) corresponds to individual bands. For example, the inset figure in Fig. 19 shows the evolution of the peak strain rate for a single band (for $\dot{\delta}_{App} = 7$ μm/s) from nucleation until it reaches the steady-state value that is being reported in the main figure. Chen
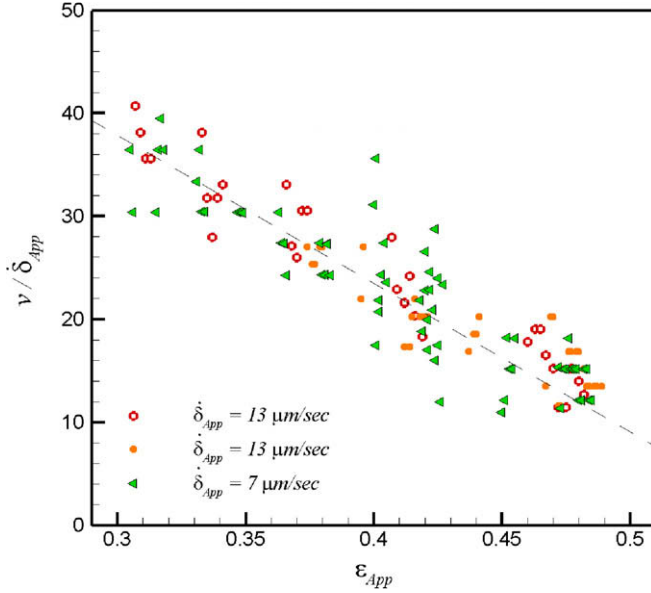
Fig. 18. Normalized steady-state band speed, $v/\dot{\delta}_{App}$, with applied strain, ε_{App}, for three separate tensile tests at cross-head speeds of $\dot{\delta}_{App} = 7$ and 13 µm/s.
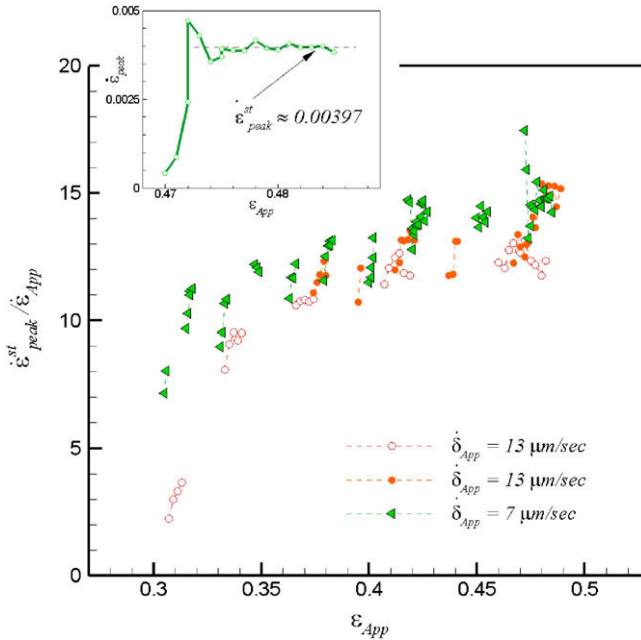

Fig. 19. Normalized steady-state peak PLC band strain rate, $\dot{\varepsilon}^{st}_{peak}/\dot{\varepsilon}_{App}$, with applied strain, ε_{App}. The peak strain rate of the bands increases from zero and then reaches a steady-state value. Inset: Evolution of the strain rate peak with ε_{App} for a typical band.

et al. (2007) estimated that the peak strain rates in the bands were as high as 100 times of $\dot{\varepsilon}_{App}$. However, Fig. 19 suggests that the peak strain rates in the bands computed with the DIC method are only 10–15 times $\dot{\varepsilon}_{App}$.

3.5. PLC effect in 1° taper geometry with 0° orientation

The interesting, although unusual behavior of the Type A PLC band nucleation and propagation events displayed in Figs. 7, 8, and 14 could not be explained on the basis of local tensile specimen geometry alone. To further investigate the effect of tensile specimen geometry on PLC band nucleation, a set of ancillary tests was conducted with TWIP specimens having the tapered geometry in Fig. 1b. Representative results from DIC post-processing are shown in Fig. 20. Fig. 20a shows a strain rate contour map with a nearly fully nucleated PLC band 5 mm to the right of the center of a tapered tensile specimen (i.e., the 5 mm "narrowest" gage width in Fig. 1b). This map is superimposed on top
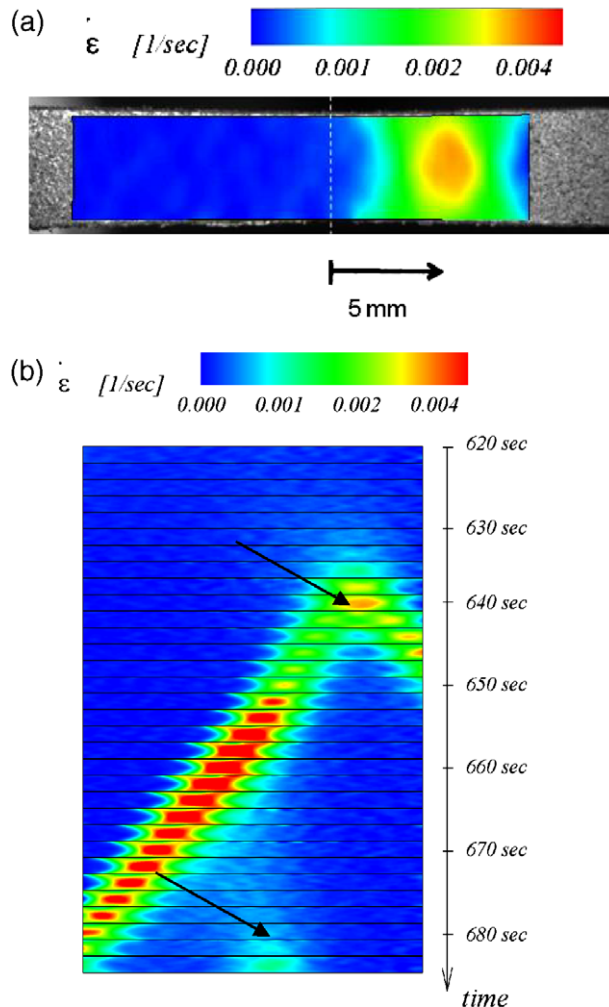

Fig. 20. (a) A strain rate contour map superimposed on digital image 353 of a tensile specimen with the 1° taper geometry in Fig. 1b. This is near the end of the nucleation of a Type A PLC band 5 mm to the right of center of the specimen. The image in (a) occurred at 640 s into the test. The vertical dashed line denotes the center of the specimen where the width is thinnest. (b) The band nucleation sequence (consistent with the displays in Figs. 11 and 14) leading up to the band in (a), which is denoted by the upper arrow, followed by band propagation towards both gripper ends. The taper is at the center of each strain rate contour map. Note that the second band nucleation event near the bottom of the sequence at 680 s occurs at the gage center where the width is smallest. This is denoted by the lower arrow.
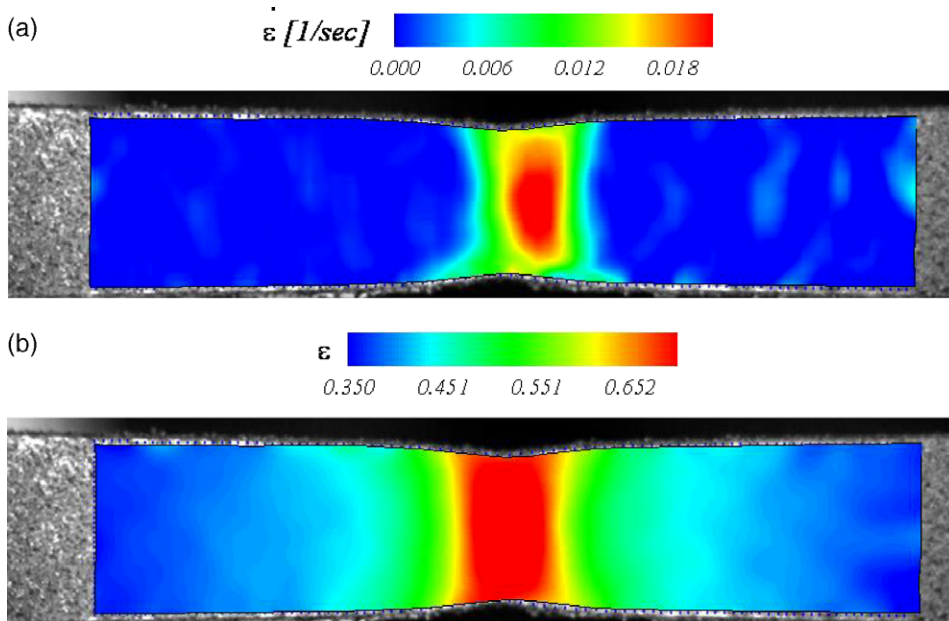
Fig. 21. (a) Strain rate contour plot superimposed on digital image 447 (i.e., the last image prior to fracture of the test from which Fig. 20 was computed) showing that PLC band propagation ends at the center of a tensile specimen with the 1° taper geometry in Fig. 1b. (b) The corresponding cumulative axial strain field at image 447 showing ∼0.65 peak true strain at the specimen center.

of digital image 353 (out of 447) of the deforming tensile specimen surface. Fig. 20b is a sequence of strain rate contour maps that shows the nucleation events prior to 640 s that lead to the band in Fig. 20a followed by band propagation towards both gripper ends. The topmost arrow denotes the image in Fig. 20a. The center of the tensile specimen (i.e., along the dashed vertical line in Fig. 1b) corresponds to the center of each map which has been compressed following the style of the strain rate contour sequences in Figs. 11 and 14. Band nucleation occurs neither at the center of the specimen nor at either of the gripper ends. This suggests that the Type A PLC bands may nucleate at heterogeneities in the TWIP steel microstructure (e.g., local texture fluctuations). As the band propagates toward the left gripper end, the peak strain rates intensify (i.e., the contours become redder) as they approach the center of the specimen. Interestingly, a second band nucleation event can be seen in the bottom two maps in the sequence in Fig. 20b. This event, which is denoted with the lowermost arrow, occurs very close to the center of the gage section center.

Fig. 21a is a strain rate contour map superimposed on image 447 of the test detailed in Fig. 20. Note that this is the final digital image recorded prior to fracture. This image shows that PLC band propagation terminates at the center of a tensile specimen with the 1° taper. Fig. 21b shows the corresponding cumulative strain contour map with a peak axial strain of ∼0.65.

4. Summary remarks

The experimental investigation detailed in this paper provided a quantitative view of spatio-temporal characteristics of the Portevin–Le Châtelier effect in an austenitic TWIP steel. Digital images were recorded from the surfaces of both straight and tapered specimens during quasi-static, room temperature tensile tests in a miniature tensile stage. Ancillary tests of straight gage TWIP specimens at higher strain rates provided results that are suggestive of nSRS. Post-processing of the images from each test with a DIC method provided direct measurement of strain fields. Care was taken to ensure

that a suitable number of images was recorded during serrations in load–time records. This was enabled through continuous monitoring of load and displacement data from the tensile stage controller electronics with a custom image acquisition algorithm. The algorithm effectively coupled image capture by a high speed digital camera with user-chosen load and displacement gradients. Of the three common PLC band types, only the Type A continuously propagating bands were observed via strain rate contour maps computed with a backwards differentiation scheme. Band velocities, when scaled by the applied displacement rate, show a nearly linear decrease with applied strain. Strained material in the wakes of earlier bands slows the movement of bands nucleated at later times. Type A PLC band nucleation, which occurred at the crests of serrations in true stress–true strain curves exhibited a quixotic nature. In straight gage specimens, band nucleation was found to occur either at a gripper end or at (or near) the gage section center beyond 0.3 true strain. In all cases, band propagation commenced at the end of each nucleation event as straining continued. Alternatively, Type A band nucleation was observed to occur between the gage section center and a gripper end in a tensile specimen with a 1° taper. These observations suggest that band nucleation is not limited to regions of geometry-induced stress concentrations (e.g., the gripper ends of a straight gage tensile specimen or the gage section center in a tapered tensile specimen). Rather, material heterogeneities that are a fraction of the specimen thickness may in fact play a crucial and as of yet poorly understood role in band nucleation. A more definitive investigation aimed at exploring the effects of such factors as TWIP steel texture evolution, other defects, and the possible roles of twinning and Mn on band nucleation will be required.

Some comments regarding implications for theoretical modeling of the intriguing TWIP PLC band nucleation and propagation behavior observed in this study are warranted. While it is not clear if any theoretical framework for the PLC effect in the open literature is adequate for TWIP steel, that due to Kok et al. (2002) is noteworthy. Here, a phenomenological PLC constitutive model due to Kubin and Estrin (1990) and McCormick and Ling (1995) is used in a polycrystal plasticity framework. Kok et al. (2002) avoid introducing "artificial" inhomogeneities that have been imposed in other models, such as those due to geometry (McCormick and Ling, 1995), an initial stress heterogeneity (Zhang et al. 2001), or perturbation of a strain hardening parameter (Becker, 1999). Rather, instabilities in the Kok et al. (2002) model arise due to spatial variations in the polycrystalline texture. Contour plots of plastic strain rate were computed for an Al–Mg alloy that show PLC band propagation. We believe that the PLC band behavior suggested in the Kok et al. (2002) model is qualitatively consistent with our experimental results. An additional issue of interest from a theoretical standpoint is whether or not their PLC constitutive model can be improved not only for the Al–Mg alloy investigated in their work but also for TWIP steel. Recent mechanistic models of DSA due to Curtin et al. (2006) and Soare and Curtin (2008) clearly suggest that the answer is yes. The impact of twinning (Oberson and Ankem 2005, 2008 and Proust et al., 2008) and Mn additions on the PLC constitutive model also require further exploration.

Acknowledgements

Appendix A. Measurement system error analysis for Young's modulus determination

Accurate Young's modulus values are vital to linear static analyses of vehicle structures, e.g., noise vibration and hashness. Determination of Young's modulus from a tensile test in which data is acquired from a precision optical system and a screw-drive tensile stage is particularly challenging

due to the small displacement range over which strains must be measured. It was found that Young's modulus values computed from the elastic portion of true stress–true strain values with the system described in Section 2 are artificially high. The reason for this pertains to the high sensitivity of the imaging system to very small out-of-plane displacements of the tensile specimen (i.e., relative to the camera lens) during elastic loading. In other words, as the tensile specimen begins to elongate under elastic loads, its surface has a subtle vertical displacement that cannot be detected visually (similar behavior occurs in larger testing systems). Such displacements are inherent to the testing equipment and are not unique to the equipment used in this research. This leads to smaller "apparent" or "as-measured" elastic strains since the associated errors are comparable to the "true" elastic strains required for determination of Young's modulus. The smaller apparent strains lead to an inaccurate Young's modulus.

To address this problem, we express the Young's modulus, E, as follows:

$$E = \frac{\sigma}{\varepsilon^*} \tag{A1}$$

where σ is the tensile stress, and ε^* is the measured or "effective" elastic strain taken directly from DIC measurements. The effective elastic strain is

$$\varepsilon^* = \varepsilon^e + \delta\varepsilon^e \tag{A2}$$

where $\delta\varepsilon^e$ is the error in true elastic strain from the measurement system. Once $\delta\varepsilon^e$ is measured, then ε^e is computed from Eq. (A2). Since the Young's modulus without this correction was larger than what we expected (for the present measurement system), we anticipated that $\delta\varepsilon^e$ is negative (i.e., the specimen undergoes a tiny displacement away from the camera lens during elastic loading) and proceed to prove this.

Two separate tests were run to determine errors in the strain measurement that are intrinsic to the measurement system (imaging system and tensile stage). Prior to the tests, two small sheets of a stiff paper, each with a small grid pattern, were placed near the gripper ends of the specimen such that they remained within view of the camera lens. This is shown in Fig. A1.

The first test involved DIC strain analysis of two static images of the grids. For this test, the camera was directed to take two images of the same grid pattern without any intentional movement of either the tensile stage or the camera. This was repeated many times and ultimately an intrinsic error in the 20–30με range (resulting from tiny vibrations in the optical system, for example) was revealed. This small error was determined not to have any effect on Young's modulus.

The next test involved loading the tensile specimen into the plastic range, gathering about 100 images, and then manually terminating the test. The purpose of this test was to determine if either or both grids undergo displacements towards the camera or away from the camera during the earliest stages of the tensile test (the small rotations of each grid as the tensile specimen is stretched have no effect on the measured strains, and the thickness of the tensile specimen itself does not decrease). These displacements are indicative of subtle errors in the measurement system. The error in the true elastic strain, $\delta\varepsilon^e$, is determined via DIC analysis of each grid pattern once the test terminates. The origin of the errors that this process quantifies can be explained with the following analogy. If one holds a
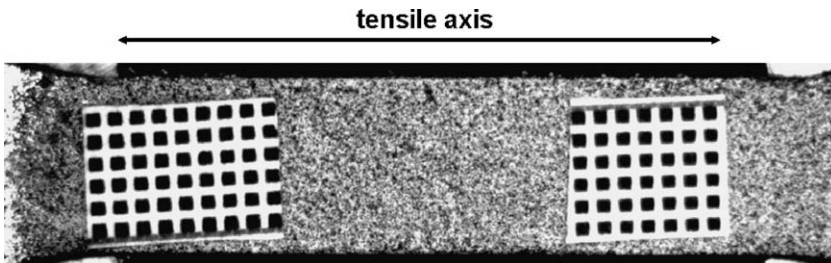

Fig. A1. TWIP straight gage tensile specimen with small calibration grids placed at either end.
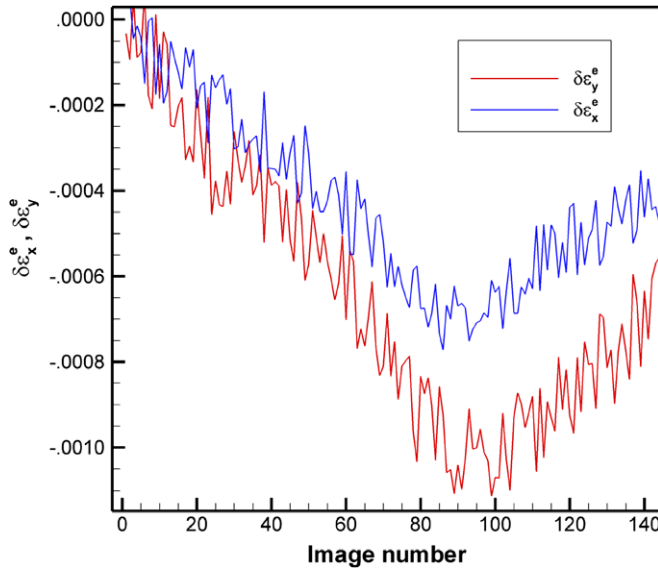
Fig. A2. Strain errors due to movement of the left grid pattern in Fig. A1 during a tensile test. The downward portions of each curve represent the loading phase. The upward portions resulted from manual unloading of the tensile specimen.

small piece of paper about 25 mm from one's eyes, and then moves it away at arm's length, there is a perceived de-magnification of the paper. In the absence of any knowledge of arm movement away from the face, this outward displacement of the note is comparable to application of uniform compressive strains (along *x* and *y*, i.e., the major axes of the paper) that effectively "shrink" its size (without wrinkling it). Clearly, any "shrinkage" of either grid pattern without an applied compressive stress (as the specimen is elongated) is truly an artifact of the measuring system. This artifact is exactly what the DIC technique detects if in fact either or both grids undergo vertical displacement once the tensile specimen begins to elongate.

Indeed $\delta\varepsilon^e$ was found to be negative from DIC analysis of the grid pattern images. This is shown in Fig. A2, which displays computed axial (i.e., along the tensile axis) and transverse (i.e perpendicular to the tensile axis) strains, $\delta\varepsilon_x^e$ and $\delta\varepsilon_y^e$, respectively, with image number from the left grid pattern in Fig. A1 (the errors from both grid patterns were nearly identical). Both strains are negative due to downward movement of each grid relative to the camera lens during elastic loading. We note that the errors in the elastic strains are around $600\mu\varepsilon$ and these will adversely affect determination of Young's modulus. The apparent "noisiness" in both curves resulted from inherent noise in the grids shown in Fig. A1 (e.g., poor edge quality between black and white features, noise from the printing process, etc.). Although this noise could be dramatically reduced with high precision calibration grids, the general linear trend during loading was sufficient to fit a function to one or both of the curves. The strain errors turn around near image 100 and move back toward zero. This resulted from manual unloading which was required to terminate the test.

An average profile was generated from the decreasing portions of the two curves in Fig. A2, $\delta\varepsilon^e$. We further assume first that $\delta\varepsilon^e$ is related to the F^e force (from the tensile stage load cell) via a "stiffness" K_2 and a small error due to any existing compressive load at the outset of straining denoted by K_1. Hence, the error due to displacement of the grids during straining of the tensile specimen in Fig. A1 is conveniently estimated by

$$\delta\varepsilon^e = K_1 + K_2 F^e \tag{A3}$$

A fit of Eq. (A3) to $\delta\varepsilon^e$ from Fig. A2 gives

$$K_1 = -8.98 \times 10^{-5} \tag{A4}$$

and

$$K_1 = -2.23 \times 10^{-7} N^{-1} \tag{A5}$$

The true elastic strains are computed by correcting the "apparent" strains computed from DIC analysis of a tensile test via

$$\varepsilon^e = \varepsilon^* - \delta\varepsilon^e \tag{A6}$$

Since $\delta\varepsilon^e$ is negative, $\varepsilon^e > \varepsilon^*$, and a smaller Young's modulus value will result.

The correction to the elastic strains in Eqs. (A3), (A4), (A5) pertain only to the TWIP steel straight gage tensile specimens investigated in this research. It is highly likely that these coefficients will change for a material other than TWIP steel or if the sheet thickness changes. Hence, the tests detailed in this Appendix must be conducted for each material tested and for each sheet gage.

References

AHSS Guidelines. 2008. Advanced High Strength Steel (AHSS) Application Guidelines Version 4. Prepared by World Auto Steel Association, Committee on Automotive Applications, World Steel Association, USA. Available from: <www.worldautosteel.org>.

Allain, S., Chateau, J.-P., Bouaziz, O., 2004a. A physical model of the twinning-induced plasticity effect in a high manganese austenitic steel. Mater. Sci. Eng. A 387–389, 143–147.

Allain, S., Chateau, J.-P., Dahmoun, D., Bouaziz, O., 2004b. Modeling of mechanical twinning in a high manganese content austenitic stainless steel. Mater. Sci. Eng. A 387–389, 272–276.

Allain, S., Cugy, P., Scott, C., Chateau, J.-P., Rusinek, A., Deschamps, A., 2008. The influence of plastic instabilities on the mechanical properties of a high-manganese austenitic FeMnC steel. Int. J. Mater. Res. 99, 734–738.

Ananthakrishna, G., Bharathi, M.S., 2004. Dynamical approach to the spatiotemporal aspects of the Portevin–Le Chatelier effect: chaos, turbulence, and band propagation. Phys. Rev. E 70. 026111–1.

Basinski, Z.S., 1957. The instability of plastic flow of metals at very low temperatures. In: Proceedings of the Royal Society of London. Series A, Math. Phys. Sci. 240 (1221), 229–242.

Bayraktar, E., Khalid, F.A., Levaillant, C., 2004. Deformation and fracture behavior of high manganese austenitic steel. J. Mater. Proc. Technol. 147, 145–154.

Becker, R., 1999. Simulating effects of dynamic strain aging with a state variable model. In: Zabaras, N., Becker, R., Lalli, L., Ghosh, S. (Eds.), The Integration of Material, Process and Product Design. Balkema, Rotterdam, pp. 77–84.

Bouaziz, O., Guelton, N., 2001. Modeling of TWIP effect on work hardening. Mater. Sci. Eng. A A319–A321, 246–249.

Brechet, Y., Hutchinson, C., 2006. Defect-induced pattern dynamic formation in metals and alloys. In: Ehrenreich, H., Spaepen, Frans (Eds.), Solid State Physics 60. Academic Press, pp. 182–285.

Chan, K.S., Chen, L.H., Lui, T.S., 1997. Serrated flow and dynamic precipitation in elevated temperature tensile deformation of Fe–Mn–Al–C alloys. Mater. Trans., JIM 38, 420–426.

Chen, L., Kim, H.-S., Kim, S.-K., De Cooman, B.C., 2007. Localized deformation due to Portevin–Le Chatelier effect in 18Mn–0.6C TWIP austenitic steel. ISIJ Int. 47, 1804–1812.

Cho, S.-H., Yoo, Y.-C., Jonas, J.J., 2000. Static and dynamic strain aging in 304 austenitic stainless steel at elevated temperatures. J. Mater. Sci. Lett. 19, 2019–2022.

Christian, J.W., Mahajan, S., 1995. Deformation twinning. Prog. Mater. Sci. 39, 1–157.

Cleveland, R.M., Ghosh, A.K., 2002. Inelastic effects on springback in metals. Int. J. Plasticity 18, 769–785.

Cottrell, A.H., 1953. A note on the Portevin–Le Châtelier effect. Philos. Mag. 44, 829–832.

Cuddy, L.J., Leslie, W.C., 1972. Some aspects of serrated yielding in substitutional solid solutions of iron. Acta Metall. Mater. 20, 1157–1167.

Cunningham, S., 1999. Effect of substitutional elements on dynamic strain aging in steel. Master's Thesis, Department of Mining and Metallurgical Engineering, McGill University, Montreal, CA.

Curtin, W.A., Olmsted, D.A., Hector Jr., L.G., 2006. A predictive mechanism for dynamic strain ageing in aluminium–magnesium alloys. Nat. Mater. 5, 875–880.

de Almeida, L.H., Emygdio, P.R.O., 1994. Activation energy calculation and dynamic strain aging in austenitic stainless steel. Scripta Metall. Mater. 31, 505–510.

de Almeida, L.H., Le May, I., Emygdio, P.R.O., 1998. Mechanistic modeling of dynamic strain aging in austenitic stainless steels. Mater. Charac. 41(4) 137–150.

De Cooman, B.C., Chen, L., Jim, H.S., Estrin, Y., Kim, S.K., Voswinckel, H., 2008. Review of the mechanical properties of high strength, high-Mn TWIP steels for automotive applications. Manuscript Prepared for the Conference on New Developments on Metallurgy and Applications of High Strength Steels, Buenos Aires, May 26–28, 2008.

Doege, E., Kulp, S., Sunderkötter, C., 2002. Properties and application of TRIP-steel in sheet metal forming. Steel Research 73, 3003–3308.

Faciu, C., Molinari, A., Dablij, M., Zeghloul, A., 1998. A new rate-type gradient-dependent viscoplastic approach for stop-and-go strain band propagation: numerical vs. physical experiments. J. Phys. IV 8, 143–150.

Frommeyer, G., Brux, U., Neumann, P., 2003. Supra-ductile and high-strength manganese-TRIP/TWIP steels for high energy absorption purposes. ISIJ Int. 43, 438–446.

Grässel, O., Krüger, L., Frommeyer, G., Meyer, L.W., 2000. High strength Fe–Mn–(Al,Si) TRIP/TWIP steels development – properties–application. Int. J. Plasticity 16, 1391–1409.

Hähner, P., 1996a. On the Physics of the Portevin–Le Chatelier effect. Part 1: The statistics of dynamic strain ageing. Mater. Sci. Eng. A207, 208–215.

Hähner, P., 1996b. On the Physics of the Portevin–Le Chatelier effect. Part 2: From microscopic to macroscopic behaviour. Mater. Sci. Eng. A20, 216–223.

Hähner, P., Ziegenbein, A., Neuhauser, H., 2001. Observation and modeling of propagating Portevin–Le Chatelier deformation bands in Cu–15 at% Al polycrystals. Philos. Mag. A 81, 1633–1649.

Hähner, P., Ziegenbein, A., Rizzi, E., Neuhäuser, H., 2002. Spatiotemporal analysis of Portevin–Le Châtelier deformation bands: theory, simulation, and experiment. Phys. Rev. B 65 (134106), 1–20.

Hector Jr., L.G., Lai, Y.H., Tong, Y.H.W., Lukitsch, M., 2007. Strain accumulation in hydrogen fuel cell membranes during a single hydration/dehydration cycle. Journal of Fuel Cell Science and Technology 4, 19–28.

Hoanga, H., Barbea, F., Queyb, R., Taleba, L., 2008. FE determination of the plasticity induced during diffusive transformations in the case of nucleation at random locations and instants. Comput. Mater. Sci. doi: 10.1016/j.commatsci.2007.07.032.

Hong, S.-G., Lee, K.-O., Lee, S.-B., 2005. Dynamic strain aging effect on the fatigue resistance of type 316L stainless steel. Int. J. Fatigue 27, 1420–1424.

Hooper, W.H.L., 1952. The influence of composition on the incidence of strain markings in aluminum alloys. J. Inst. Metals 81, 563–568.

Horvath, C.D., Fekete, J.R., 2004. Opportunities and challenges for increased usage of advanced high strength steels in automotive applications. In: Proceedings of International Conference on Advanced High Strength Sheet Steels for Automotive Applications, pp. 3–10.

Iker, M., Gaude-Fugarolas, D., Jacques, P.J., Delannay, F., 2007. Improvement of the mechanical properties of manganese steels by combination of precipitation hardening and mechanical twinning. Adv. Mater. Res. 115–117, 852–857.

Ilola, R., Kemppainen, M., Hannienen, H., 1999. Dynamic strain aging of austenitic high nitrogen Cr–Ni and Cr–Mn steels. Mater. Sci. Forum, 407–412.

Jenkins, C.F., Smith, G.V., 1969. Serrated plastic flow in austenitic stainless steel. Trans. Met. Soc. AIME 245, 2149–2156.

Kim, D.W., Ryu, W.-S., Hong, J.H., Choi, S.-K., 1998. Effect of nitrogen on the dynamic strain ageing behavior of type 316L stainless steel. J. Mater. Sci. 33, 675–679.

Klose, F.B., Weidenmuller, J., Ziegenbein, A., Hahner, P., Neuhauser, H., 2004a. Plastic instabilities with propagation deformation bands in Cu–Al alloys. Philos. Mag. A84, 467–480.

Klose, F.B., Ziegenbein, A., Hagemann, F., Neuhauser, H., Hahner, P., Abbadi, M., Zeghloul, A., 2004b. Analysis of Portevin–Le Chatelier serrations of Type B in Al–Mg. Mater. Sci. Eng. A 369, 76–81.

Kok, S., Beadoin, A.J., Tortorelli, D.A., Lebyodkin, M., 2002. A finite element model for the Portevin–Le Châtelier effect based upon polycrystal plasticity. Model. Simul. Mater. Sci. Eng. 10, 745–763.

Krajewski, P.E., 2005. The warm ductility of commercial aluminum sheet alloys, SAE 2005-01-1388.

Krauss, G., 1990. Steels – Heat Treatment and Processing Principles. ASM International, Materials Park, OH.

Kubin, L.P., Estrin, Y., 1990. Evolution of dislocation densities and the critical conditions for the Portevin–LeChâtelier effect. Acta Metall. Mater. 38, 697–708.

Kubin, L.P., Ananthakrishna, G., Fressengeas, C., 2002. Comment on "Portevin–Le Chatelier effect". Phys. Rev. E 65, 65–66.

Kyriakides, S., Miller, J.E., 2000. On the propagation of Lüders bands in steel strips. ASME J. Appl. Mech. 67, 645–654.

Larsson, R., 2007. Constitutive Modeling of High Strength Steel. Master Thesis in Solid Mechanics, Linköping University, Institute of Technology, Dept. Mech. Eng., SE-581 83, Linköping, Sweden.

Lebyodkin, M., Dunin-Barkowskii, L., Brechet, Y., Estrin, Y., Kubin, L.P., 2000. Spatio-temporal dynamics of the Portevin–Le Chatelier effect: experiment and modeling. Acta Mater. 48, 2529–2554.

Mannan, S.L., Samuel, K.G., Rodriguez, P., 1983. Dynamic strain ageing in type 316 stainless steel. Trans. Indian Inst. Metals 36, 313–320.

McCormick, P.G., 1972. A model for the Portevin–Le Châtelier effect in substitutional alloys. Acta Metall. Mater. 20, 351–354.

McCormick, P.G., Ling, C.P., 1995. Numerical modeling of the Portevin–Le Châtelier effect. Acta Metall. Mater. 43, 1969–1977.

Oberson, P.G., Ankem, S., 2005. Why twins do not grow at the speed of sound all the time. Phys. Rev. Lett. 95 (165501), 1–4.

Oberson, P.G., Ankem, S., 2008. The effect of time-dependent twinning on low temperature (<0.2 Tm) creep of an alpha-Titanium alloy. Int. J. Plasticity. doi: 10.1016/j.ijplas.2008.06.002.

Owen, W.S., Grujicic, M., 1998. Strain aging of austenitic Hadfield manganese steel. Acta Mater. 47, 111–126.

Perez, R., Benito, J.A., Prado, J.M., 2005. Study of the inelastic response of TRIP steels after plastic deformation. ISIJ Int. 45 (12), 1925–1933.

Phillips, V.A., Swain, A.J., Eborall, R., 1952. Yield-point phenomena and stretcher-strain markings in aluminum–magnesium alloys. J. Inst. Metals 81, 625–647.

Pink, E., Kumar, S., 1995. Patterns of serrated flow in a low-carbon steel. Mater. Sci. Eng. A 201, 58–64.

Proust, G., Tomé, C.N., Jain, A., Agnew, S.R., 2008. Modeling the effect of twinning and detwinning during strain-path changes of magnesium alloy AZ31. Int. J. Plasticity. doi: 10.1016/j.ijplas.2008.05.005.

Rizzi, E., Hahner, P., 2004. On the Portevin–Le Chatelier effect: theoretical modeling and numerical results. Int. J. Plasticity 20, 121–165.

Robinson, J.M., 1994. Serrated flow in aluminum alloys. Int. Mater. Rev. 39, 217–227.

Savic, V., Hector Jr., L.G., 2007. Tensile deformation and fracture of press hardened boron steel using digital image correlation. SAE Transactions 2007-01-0790, 2007.

Savic, V., Hector Jr., L.G., Fekete, J.R., 2008. Digital image correlation study of plastic deformation and fracture in fully martensitic steels. Exp. Mech. doi: 10.1007/s11340-008-9185-6.

Scott, C., Allain, S., Farel, M., Guelton, N., 2006. The development of a new Fe–Mn–C austenitic steel for automotive applications. La Revue de Metalliurgie-CIT 103, 293–302.

Serajzadeh, S., 2003. Serrated flow during warm forming of low carbon steels. Mater. Lett. 57, 4515–4519.

Shi, L., Northwood, D.O., 1995. The mechanical behavior of an ASI type 310 stainless steel. Acta Metall. Mater. 43, 453–460.

Shiekhelsouk, M.N., Favier, V., Inal, K., Cherkaoui, M., 2009. Modeling the behaviour of polycrystalline austenitic steel with twinning-induced plasticity effect. Int. J. Plasticity 25, 105–133.

Smith, B.W., Li, X., Tong, W., 1998. Error assessment for strain mapping by digital image correlation. Exp. Tech. 22, 19–21.

Soare, M., Curtin, W.A., 2008. Solute strengthening of both mobile and forest dislocations: the origin of dynamic strain aging in fcc metals. Acta Mater. 56, 4046–4061.

Standard test methods for tension testing of metallic materials, designation E 8/E 8M. ASTM, 100 Barr Harbor Drive, P.O. Box C700, West Conshohocken, PA, 19428-2959.

Tamhankar, R., Plateau, J., Crussard, C., 1958. Etude de la déformation plastique a chaud d'un fer doux et d'une austénite stable au nickel-chrome. Rev. Métall. 55, 383–400.

Tao, H., Tong, W., Hector Jr., L.G., Zavattieri, P.D., 2008. Uniaxial tensile and simple shear behavior of resistance spot welded dual-phase steel joints. ASM J. Mater. Eng. Perform. 17, 517–534.

Tong, W., 1997. Detection of plastic deformation patterns in a binary aluminum alloy. Exp. Mech. 37, 452–459.

Tong, W., 1998. Strain characterization of propagative deformation bands. J. Mech. Phys. Solids 46, 2087–2102.

Tong, W., 2004. An adaptive backward image correlation technique for deformation mapping of a growing crack in thin sheets. Exp. Tech. 28 (3), 63–67.

Tong, W., 2005. An evaluation of digital image correlation criteria for strain mapping applications. Strain 41, 167–175.

Tong, W., Tao, H., Zhang, N., Hector Jr., L.G., 2005a. Time-resolved strain measurements of Portevin–Le Châtelier bands in aluminum using a high speed digital camera. Scripta Mater. 53, 87–92.

Tong, W., Tao, H., Jiang, X., Zhang, N., Marya, M., Hector Jr., L.G., Gayden, X.Q., 2005b. Deformation and fracture of miniature tensile bars with resistance spot weld microstructures: an application of digital image correlation to dual-phase steels. Metall. Mater. Trans. A 36, 2651–2669.

Tong, W., Hector Jr., L.G., Dasch, C., Tao, H., Jiang, X., 2007. Local plastic deformation and failure behavior of ND:YAG laser welded AA5182-O and AA6111-T4 aluminum sheet metals. Metall. Mater. Trans. A 38, 3063–3086.

Tong, W., Xuan, Y., Yao, H.A. 2008. An improved technique for tensile testing of sheet metals. In: Proceedings of the XIth Int. Congress and Exposition of the Society for Experimental Mechanics, June 2–5, 2008, Orlando, Fl, 1-2, Society for Experimental Mechanics, Bethel, CT.

Tong, W., Zhang, N., 2001. An experimental investigation of necking in thin sheets. Proceedings of the ASME Manufacturing Engineering Division MED 12 (2001), 231–238.

Tong, W., Zhang, N., 2007. On the serrated plastic flow in an AA5052-H32 sheet. ASME J. Eng. Mater. Tech. 192, 332–341.

Van den Beukel, 1975. Theory of the effect of dynamic strain aging on mechanical properties. Phys. Stat. Sol. A 30, 197–206.

Zhang, Q., Jiang, Z., Jiang, H., Chen, Z., Wu, X., 2005. On the propagation and pulsation of Portevin–Le Châtelier deformation bands: an experimental study with digital speckle pattern metrology. Int. J. Plasticity 21, 2150–2173.

Zhang, S., McCormick, P.G., Estrin, Y., 2001. The morphology of Portevin–Le Chatelier bands: finite element simulation for Al–Mg–Si. Acta Mater. 49, 1087–1094.